ATL-TILECAL-PUB-2007-008
14 December 2007

Measurement of Pion and Proton Longitudinal Shower Profiles up to 20 Nuclear Interaction Lengths with the ATLAS Tile Calorimeter

H. Hakobyan, M. Simonyan (YerPhI, Armenia)
T. Carli, A. M. Henriques-Correia (CERN, Switzerland)

Abstract

The response of pions and protons in the energy range of 20 to 180 GeV produced at CERN's SPS H8 test beam line in the ATLAS iron-scintillator Tile hadron calorimeter has been measured. The test-beam configuration allowed to measure the longitudinal shower development for pions and protons up to 20 nuclear interaction lengths. It is found that pions penetrate deeper in the calorimeter than protons. However, protons induce showers that are wider laterally to the direction of the impinging particle. Including the measured total energy response, the pion to proton energy ratio and the resolution, all observations are consistent with a higher electromagnetic energy fraction in pion induced showers. The data are compared with GEANT4 simulations using several hadronic physics lists. The measured longitudinal shower profiles are described by an analytical shower parameterisation within an accuracy of $5 - 10\%$.

Introduction

The Large Hadron Collider (LHC) presently built at CERN will collide protons with an energy of 7 TeV. The resulting high center of mass energy will open a new chapter for particle physics exploring the high energy frontier. Calorimeters measure charged and neutral particles produced in the collision.

Hadronic calorimeters have the main task to measure the energy and directions of jets, sprays of hadrons of various species that emerge from the hard parton parton scattering. Their hermeticity allows in addition to measure the missing transverse energy and therefore to partly reconstruct particles that are escaping detection. The understanding of the calorimeter response to hadrons and of their shower development is crucial to achieve the best possible performance of the energy measurement.

While usually the calorimeter response is tested using single pions testbeams, in the colliding beam experiment, jets are measured. Differences in the response of pions, kaons, protons and neutrons (and the corresponding antiparticles and other rare mesons and hadrons) are assumed to be small or described by the Monte Carlo simulation.

In 1994, however, it was pointed out that the response of non-compensating calorimeters to pions and protons is slightly different [1], since the underlying mechanism of the first few interactions of the hadron in the calorimeter is different. Based on Monte Carlo simulations a phenomenological model was developed that predicted the same energy depositions of hadronic nature for pions and protons, but more electromagnetic energy depositions and larger fluctuations in the electromagnetic energy fraction in the case of pions. These effects were experimentally confirmed in 1998 [2].

In this note, we study the response of the Tile Calorimeter (TileCal), located in the barrel part of the ATLAS detector, to pions and protons in the energy range of 20 to 180 GeV produced at the CERN SPS H8 test beam line. The data have been taken in the year 2002.

The TileCal consists of steel plates used as absorber material and scintillating tiles used as active medium. The new feature of the TileCal design is the orientation of the scintillating tiles which are placed in planes perpendicular to the colliding beams. However, for the runs analysed here a special non-projective configuration of the test beam set-up has been used where the beam direction is perpendicular to the scintillating tiles ("90 degree configuration"). This configuration allows almost full shower containment and makes it possible to measure shower profiles up to 20 nuclear interaction lengths[1] (λ).

Previously, in the energy range of 10 - 140 GeV the longitudinal shower pro-

[1] We use throughout this analysis an effective nuclear interaction length for the Tile calorimeter $\lambda = 20.55$ cm., calculated using the known fraction of materials used in the detector construction and their nuclear interaction lengths.

files for an iron-scintillator structure have been studied for the CDHS calorimeter [3], which had alternating scintillator and irons layers of 5 mm and 25 mm (compared to 3 mm and 14 mm in TileCal) and whose readout cells consisted of 5 scintillator-iron layers, whereas the typical TileCal readout cells was about 30 cm twice as long. The CDHS calorimeter was 240 cm long in the beam direction, to be compared to 564 cm for the TileCal Barrel modules in the 90 degree configuration.

In a recent publication of the TileCal collaboration the longitudinal shower profile has been measured for prototype modules[2], having a depth of 180 cm (9 λ) and coarse granularity [4].

As an important part of the current study the results are compared to Monte-Carlo (MC) simulations using several hadronic physics models available in the GEANT4 [5] framework. Our detailed measurements might contribute to test existing simulation packages and to guide their future development such that the stringent requirements to correctly model the calorimeter response, and in particular the hadronic shower development, imposed by the LHC physics programs, can be reached.

The paper is organized as follows. In Section 1, the TileCal, test beam set-up and the beam line detectors are briefly described. The Monte Carlo simulation and the various hadronic interaction lists are described in Section 2. The event selection and particle identification is presented in Section 3. In Section 4 the measurements and the data analysis are described and compared to Monte Carlo simulations. The measurement of the total energy and the energy resolutions for pions and protons are described in Section 4.2. In addition, the shapes of the total energy spectra distribution of proton and pions are compared. The measurement of the longitudinal shower profile and an estimator for the lateral shower spread are presented in Section 4.3 and in Section 4.4. Data are compared to MC simulations in Section 4.5.

In Section 5.1 the electromagnetic fraction contained in pion and proton induced showers is extracted using a phenomenological model. An analytical parameterization to describe the mean longitudinal shower profile is presented in Section 5.2. The measured longitudinal shower profiles are corrected for the projective form of the cell geometry in Section 5.3 and the free parameters of the mean longitudinal shower profile parameterization are adjusted to the mean unfolded longitudinal energy profile Section 5.4. Special emphasis is put on differences between protons and pions. The results obtained using the TileCal in this analysis are compared to measurements with the CDHS calorimeter in Section 5.5.

Based on the analytical parameterisation of the shower profile a determina-

[2]These measurements have been performed in projective geometry. This means that the particles enter the calorimeter as they would do in the ATLAS detector, if they were produced at the proton proton interaction point.

tion of the mean longitudinal leakage is presented in Section 6. In this section the mean longitudinal leakage is also compared to the longitudinal leakage defined as the shift of the peak of the total energy distribution obtained from a Gaussian fit. The energy and angular dependence of the longitudinal leakage is determined and parameterized. In addition, the energy resolution as a function of the calorimeter depth is presented.

1 Experimental Set-up

1.1 The Tile Barrel Calorimeter

The iron-scintillator media of the TileCal modules is made of 4 mm and 5 mm thick iron plates sandwiched by 3 mm thick scintillator tiles, with a periodicity of 18 mm. The total thickness of the iron and the scintillator in a period is 14 mm and 3 mm, respectively. The tiles are oriented perpendicularly to the modules length such that the Barrel Module is extended over 307 periods. Each side of the scintillating tiles is readout by a single wave length shifting (WLS) fiber. The fibers are grouped together, separately for each side, forming a cell, that is readout by two photomultipliers (PMT).

Each TileCal module is one of 64 azimuthal segments of the complete Barrel and Extended Barrel assembly of the Tile calorimeter in ATLAS (see for details [6]). The Barrel Module segmentation into the cells is shown in Fig. 1. It is driven by the requirement of projectivity in the η-plane[3] and in the radial direction (ϕ). The TileCal has a granularity of cells spanning $\Delta\eta = 0.1$ and $\Delta\phi = 2\pi/64 = 0.1$. Eleven tile sizes are used in the structure of the Barrel Modules, grouped into the clusters of 3+6+2 tiles, defining three radial samplings A, BC and D with depths of 1.5, 4.1 and 1.9 λ at $\eta = 0$, respectively.

1.2 Test Beam Set-up and Beam Line Detectors

The H8 test beam line at the SPS accelerator of CERN is instrumented with a set of beam detectors: scintillator trigger counters (S1-S3), wire chambers (BC1-BC2) measuring the lateral x and y position of the beam particles and a helium filled threshold Cherenkov counter. The scanning table carrying the modules was used to reproduce the angles of incidence of particles originating from the LHC interaction region.

The layout of the TileCal modules in the H8 test beam line area is shown in Fig. 2. It consists of one production Barrel Module, 5.64 m long, two production

[3]The η and ϕ directions are chosen with respect to a reference frame with cylindrical coordinates having its origin in the virtual proton-proton interaction point in ATLAS. In this coordinate system the z-axis is defined along the beam axis. The ϕ and θ angles are the azimuthal and polar angles. The pseudo-rapidity is defined by $\eta = -\log\tan\theta/2$.

modules of the Extended Barrel, 2.93 m long, which are stacked together on top of the prototype Barrel Module 0.

The Extended Barrel modules are not used in the measurement of the longitudinal shower profile due to the difficulty of accounting for the large gap (equivalent to two barrel layers) between two modules in the test beam set-up. Instead, the energy measured in the Barrel Module 0 is multiplied by a factor of two[4].

As indicated in Fig. 2 the beam impinges from the side of the production Barrel Module, perpendicularly to the scintillating tiles. The direction of the beam is defined to be the x-axis. The beam impact point has been chosen to be on the center of the fifth tile row of the BC cell. This choice takes advantage of the relatively fine longitudinal segmentation of the BC cells while giving good lateral containment of the showers, because the distance from the beam axis to the exit of the bottom Module 0 and the top of the EB Module is approximately 2 λ.

Longitudinally showers are fully contained in the calorimeter, since no energy is observed in the last layers of the modules. The lateral containment of the shower in the test beam set-up is about 99% as shown in Section 5.1.

2 Monte Carlo Simulation Tools

The simulation of the calorimeter modules was performed within the ATLAS software framework ATHENA[5] using the GEANT4 simulation toolkits [5]. The detailed shower development follows all particles with a range larger than 1 mm. Besides purely electromagnetic processes, also hadron interactions and photo-nuclear interactions were simulated.

Within the GEANT4 simulation framework several models can be used to simulate the interaction of particles with matter. The applicability of the model depends on the particle type, the energy range and the target material. There is also the possibility to use different models for the same particle type and energy range. A "physics list" is a consistent collection of models that covers the interaction of all particles in the whole energy range from thermal energies to the several TeV range. Therefore, depending on the application and on the required physics performance and the available computing time, different physics lists can be chosen.

In this study, four different physics lists have been used which are recom-

[4]Taking into account that the direction of initial particle is a symmetry axis and the distance from the axis to Module 0 and Extended Barrel module is equal, this procedure measures correctly the mean energy and the average longitudinal shower profile. However, the resolution is made somewhat worse.

[5]Version 12.0.1 has been used.

mended for calorimeter studies at LHC energies[6]:

The physics list LHEP employs parameterization-driven models for all hadronic interactions using measured and extrapolated reaction cross-sections, particle spectra and multiplicities for the final state. Several parameters have been tuned in a global fit to describe a large number of hadron-hadron scattering data. It contains the Low Energy Parameterized (LEP) model for interaction of hadrons for low energies and the High Energy Parameterized (HEP) model for higher energies[7].

As a result, the LHEP physics list provides a fast simulation, but baryon and meson resonances are not produced and the secondary angular distributions for low energy reactions of $O(100$ MeV) cannot be described in detail. This model is a reimplementation of the GHEISHA model in GEANT3.21 [10].

The second physics list QGSP employs the well-known formalism of the quark-gluon string (QGS) model for soft and fast 'punch-through' interactions of the projectile with nucleons of the nuclear medium. The string excitation cross-sections are calculated in the quasi-eikonal approximation. QGSP uses Barashenkov's pion cross-section [11] and the Wellisch-Axen systematics for nucleon induced reactions [12]. At low energies QGS is not applicable and the LEP model is used instead[8]. The precompound model is used for de-excitation of a nucleus left in an excited state after energetic interaction.

In both physics lists, QGSP and LHEP, the Bertini intra-nuclear cascade model for hadron-nucleus interactions can be added (QGSP_BERT and LHEP_BERT). In this case the strong interaction of hadrons below 10 GeV is simulated according to the Bertini model [13] [9]. In this model the projectile and induced secondaries are transported along straight lines through the nuclear medium (approximated by concentric, constant-density shells) and interact using the free hadron-nucleon total cross-section. At the shell boundaries a particle can be reflected or transmitted. As cascade collisions occur, excited residual nuclei are formed which can then evaporate neutrons or alpha particles and can radiate photons due to inter-nuclear transitions, as well as undergo weak decay with subsequent de-excitation.

The simulation of the TileCal scintillators includes the effects of photo statis-

[6] With the GEANT4 package they are named: LHEP_GN 2.5 , QGSP_GN 2.6, QGSP_BERT 1.1 and LHEP_BERT 1.2.

[7] The code applies the HEP (or the LEP) model with a probability that increases from zero to 1 (or decreases from 1 to zero) linearly as the hadron energy increases from 25 GeV to 55 GeV.

[8] The QGS (LEP) model is always used for energies above 25 GeV (below 12 GeV). Hadrons between 12 and 25 GeV are treated by either model, with the choice being made event by event by a linearly varying probability, as in the previous case.

[9] The Bertini model is fully used up 9.5 GeV. The LEP model is fully used for energies larger than 9.9 GeV. For energies between 9.5 and 9.9 GeV a choice between the two models based on a linearly increasing probability is made.

tics in the photomultipliers. However, no attempt is made to describe the detailed optical properties of the scintillating tiles and the read-out fibres. The electronic noise was extracted from experimental data using randomly triggered events and added incoherently to the energy of each PMT in the MC samples. Coherent noise is not simulated, but known to be relatively small.

A sample of 10000 events was simulated for each physics list and for each beam energy and particle type.

3 Data Set and Event Selection

3.1 Data Set and Event Selection

The data analyzed here were taken in June and July of 2002 and cover the energy range from 20 to 180 GeV. The following runs have been used: 200616, 210563, 210487, 210483, 210435 and 210436, 210260, 200147, 200180. TileCal production Barrel modules JINR-34 and JINR-55 were exposed to particle beams during June and July respectively.

Events in the tails of the lateral beam profile are eliminated with the help of the beam chambers. The response of the chambers is fitted with a Gaussian and all events within three standard deviations around the mean are accepted. These cuts reduce the momentum spread of the beam and decrease the acceptance for events, where a hadron decays or interacts early in the material of the H8 beam line before entering the calorimeter.

In each of the scintillator counters S1-S3, a signal compatible with the one from a minimum ionizing particle is required in order to remove multiple hits from accidental coincidences of beam particles and to reject early showering hadrons.

The reconstructed time and energy of all PMTs are used to reconstruct the energy weighted event time. All events within three standard deviations around the mean are accepted.

3.2 Particle Identification

The hadron beams produced at the H8 beam line contain in general a mixture of electrons, muons, pions, protons and possibly also kaons, depending on the beam energy, the used target (primary, secondary or tertiary) and the beam line optics.

It is therefore necessary to identify the type of the particle impinging to the calorimeter and to determine the purity of the selected sample. If possible, external detectors like the Cherenkov counter are used for particle identification. However, it is also necessary to use the information from the calorimeter itself. In this case a bias on the calorimeter measurement is introduced and needs to

be carefully evaluated either by studying the effect of the cut in the data or by using a MC simulation.

It has been checked that runs with nominally different particle beams give the same results after particle identification. The number of events for each particle type, selected as described and for each beam energy is summarized in Table 1.

3.3 Pion and Proton Identification

The Cherenkov counter is used to discriminate pions from protons. The distribution of the Cherenkov counter signal (in ADC counts) is shown in Fig. 3 for beam energies of 50, 100 and 180 GeV.

The peak in the low signal region is compatible with the pedestal distribution and corresponds to protons [10]. The shape of the proton distribution can therefore be well modeled with a Gaussian.

The broad distribution, peaked at larger signals, is due to pions and muons. Its shape can be described by a Poisson distribution with a mean value that corresponds to the 2 to 4 photoelectrons registered by the photomultiplier (depending on the pressure settings). Since the distribution is also smeared by the finite resolution and truncated at low values by the electronics threshold, it cannot be described analytically. A noticeable fraction of the events does not generate a signal in the Cherenkov counter and therefore exhibits a tail that extends also to the pedestal zone.

To estimate the residual contamination of pions in the sample of protons and the contamination of protons in the sample of pions the following method was used: Muon events, selected by requiring a small energy deposition in the calorimeter, are used to estimate the shape of the pion distribution in the low signal region (see open circles in Fig. 3). Due to the small mass difference of muons and pions (as compared to the one between pions and protons), muons are expected to closely reproduce the pion distribution of the Cherenkov response in the full signal range. Together with the Gaussian describing the proton peak the muon distribution is scaled to describe the measured hadron Cherenkov signal distribution. The dashed and the dotted line in Fig. 3 are the result of this fit. Hadron and muon Cherenkov signal distributions are compatible within statistical errors in the region (large ADC counts), where no contribution from protons is expected. Therefore, systematics uncertainty resulting from muon-pion mass difference is negligible.

Comparing hadron and muon Cherenkov signal distributions in the region (large ADC counts), where no contribution from protons are expected, we conclude that the shapes of the distributions are compatible within statistical errors.

[10] The threshold (gas pressure) of the Cherenkov counter was set such that protons give no signal. It also slightly cuts the expected pion spectrum, but keeps the efficiency above 90%.

Therefore systematics uncertainties resulting from muon-pion mass difference are negligible.

From this fit the pion (proton) contamination in the proton (pion) sample can be estimated by calculating the number of events below (above) the chosen cuts.

This method naturally takes into account the inefficiencies of the Cherenkov counter that will lead to pions or muons contribution in the proton sample. The inefficiency can be assumed to be independent of pions and muons and therefore no assumption on the shape of the pion distribution in the low region is necessary.

The pion contamination in the sample of protons is summarized in Table 1. Proton contamination in the pion sample is found to be negligible at all energies. A sharp increase of the contamination is observed at 180 GeV that is a consequence of non-optimal pressure settings, leading to a visible efficiency loss of pions.

Since at $E = 180$ GeV the contamination is quite large, all observables measured for protons are corrected using the determined fraction of pions in the proton sample and the measured observables for pions. This is possible, because the proton contamination in the pions sample, as evaluated, is seen to be comparatively small.

The shape of the Cherenkov counter spectra does not leave much room for a third possible hadron species in the beam, kaons in particular. Their contamination in the beam line was estimated by MC simulations to be less than about 5 % [7] at 180 GeV and less at lower energy.

3.4 Electron and Muon Rejection

To remove electrons and muons in the pion beam no external detector was available. The rejection has to be based on the topology of the energy depositions in the calorimeter.

Electrons are rejected using the average energy density [16] defined as

$$AvD = \frac{1}{N} \sum_i \frac{E_i}{V_i}, \tag{1}$$

where N is number of cells above a certain energy threshold[11], and E_i and V_i are the energy and the volume of the cell i, respectively.

As an example, the distribution of the average energy density at 50 GeV is presented in the Fig. 4. It is fitted with the shapes of the simulated pion and

[11] For energies $E \geq 50$ GeV, only cells having more than about 1% of the total measured energy enter in the sum of eq. 1. For lower energies, the best separation is achieved, if the cell threshold is increased to 50 % of the total measured energy. These optimal thresholds have been evaluated with a Monte Carlo simulation.

electron distributions varying their relative weights. The pion distribution was modeled using an equivalent number of events simulated with the LHEP_BERT and QGSP_BERT physics lists [12].

To discriminate pions from electrons a cut value corresponding to the minimum of the average energy density distribution is applied. This value slightly depends on the beam energy and is adjusted for each energy.

The electron contamination in the 20 GeV pion sample is evaluated to be less than 0.5 %, while keeping the pion efficiency of 98.7%. At 50 GeV the electron contamination is already as low as 0.2% and further decreases towards higher beam energies.

To reject muons in the pion sample the total measured energy in the calorimeter is used. The cut is chosen such that no pion event is removed. Since the measured energy distribution is symmetric thanks to the good energy containment of the set-up, the amount of pions or protons with an energy below this cuts can be estimated by comparing the high energy to the low energy tail of the energy distribution of pions or protons.

Such a cut removes the overwhelming fraction of muon events, but does not allow to identify the rare cases where muons induce showers with large, mainly electromagnetic energy deposits through the processes of bremsstrahlung, pair production and knock-on of delta rays.

Since the cross-section of those processes is very low, the distribution of showering muons events along the beam direction is rather uniform compared to the sharp increase of the hadron interaction probability, that scales as $(1 - \exp(-x/\lambda))$. Therefore, if only a cut on the total energy is used, muons that deposit a large amount of energy in one or few cells can be misclassified as hadrons and the longitudinal profile at the end of hadronic shower may be noticeably overestimated.

The mentioned features can be exploited by defining a likelihood that a given event is compatible in each cell with the expected muon energy distribution obtained from the GEANT4 [5] simulation that models all electromagnetic radiative processes[13]. The likelihood uses the product of the probabilities of each cell. To further enhance the pion muon separation the likelihood is in addition divided by the probability that a hadron does not interact until a given depth that is given by $\exp(-x/\lambda)$. The first cell in the trajectory of the initial particle where the signal exceeds a given threshold is considered to be the cell

[12] As shown in Section 4.5 the measured longitudinal profile is in between the prediction of QGSP and LHEP (within 20%) when adding the Bertini cascade. In addition, the lateral shower spread is well described. Therefore, LHEP_BERT and the QGSP_BERT are used to describe the average energy density and to estimate the systematic uncertainties introduced by the cut to reject electrons.

[13] In the version used in this analysis photo-nuclear interaction induced by muons have not been simulated. This should, however, not be a problem, since the cross-section for this reaction is very low.

	pion sample				proton sample	
E_{beam} [GeV]	π	p [%]	e [%]	μ [%]	p	π [%]
20	55580	–	≤ 0.53	≤ 0.02	–	–
50	11915	≤ 0.02	≤ 0.22	≤ 0.02	7158	2.9 ± 0.2
100	11104	≤ 0.03	≤ 0.20	≤ 0.03	19871	0.77 ± 0.06
180	16171	≤ 0.02	≤ 0.19	≤ 0.04	24999	12.6 ± 0.2

Table 1: Summary of the number of proton and pion events in the data set. Also shown are the numbers of the determined contaminations in the proton and pion sample. The contamination of electrons and muons in the proton sample is very small and therefore not given. At 20 GeV only a negative beam was available (with no proton contamination). The numbers with a less equal sign in front are an upper limit on the contamination.

where the first hadronic interaction happens.

As an example, the resulting muon likelihood distribution for a beam energy of 100 GeV is shown in Fig. 5. In Fig. 5a all events are shown, while in Fig. 5b the events above the cut on the total energy are shown. The likelihood provides a very good separation. Two separate peaks are clearly visible, the one on the left corresponding to pions and the one on the right to muons.

To discriminate muons from pions a cut near the minimum of the likelihood distribution is chosen for each energy.

Superimposed on Fig. 5 as lines are the results of MC simulations. The dotted line shows a pion simulation and the dashed line a muon simulation. An appropriate mixture of these MC simulations obtained by varying their relative weights is shown as a solid line. It is remarkable that the MC simulation describes well the shape of the likelihood distribution in the data, in particular also the hadronic part[14].

Therefore the MC simulation can be used to evaluate the purity of the pion sample. To reject muons in the pion sample, only events below a cut corresponding to the minimum of the likelihood are accepted. In addition the cut on the total deposited energy further reduces the very few events where muons pass the requirement on the likelihood.

The electron and muon contaminations in the proton sample were also evaluated. They are negligible, since the Cherenkov counter rejects almost all of them.

Upper limits on the contamination of muons and electrons in the pion sample for each beam energy are given in Table 1.

[14]All hadronic physics lists described in Section 2 give similar results for this observable. To increase the number of simulated events all physics lists are used in the figure.

4 Data Analysis and Comparison with Simulation

4.1 Calibration and Corrections

The electronics calibration of the TileCal for the data taking period analysed here is described in detail in ref. [7]. For a representative sample of 11 % of in total 192 modules produced for the ATLAS detector, a module-to-module variation of response of 3 % using electron beams [26] and 1.4 % using hadron beams [25] has been measured. The cell-to-cell variation within one module is 3 % as determined using electrons. The linearity of the calorimeter response to electrons as a function of beam energy is better than 1 %. Most of the results in ref. [7] are obtained with beam impinging in the projective geometry, relevant for the understanding of the calorimeter response in proton-proton collisions. For the configuration used in this analysis (90 degree) a response variation of 2.5 % has been found using muon beams and 4.5 % using electron beams.

Random trigger events are used to calculate the residual pedestals for each PMT. The obtained mean values are subtracted from the PMT signal.

The functioning of the PMTs is checked by selecting muons in the hadron beams impinging at various lateral positions on the calorimeter. Since muons deposit uniformly along their path they are a good tool to check the PMT response (calibration, noise, etc.).

Only a few cases of PMT with unexpected low signals were observed. In this case the PMT energy was set to zero and the energy of the PMT reading out the opposite side of the cell was multiplied by a factor of 2.

In the 2002 test beam set-up half of the Barrel Module 0 had no read-out electronics. To overcome this limitation, for each beam energy two runs were taken, with the beam hitting opposite sides of the production Barrel Module. In this manner, the symmetry of the set-up around $\eta = 0$ allowed to measure, in separate runs, the average energy depositions in the upstream and downstream halves of Module 0. The mean energy deposition as well as the longitudinal shower profile can then be on average reconstructed from these two measurements.

To measure the total energy distribution the run where the beam impinges on the active part of Module 0 is used and the mean total energy is then corrected by the energy deposited in the non-working part of Module 0 that can be obtained from the run where the beam impinges on the side of the non-working part. This correction is rather small. It is clear, however, that the RMS can not be corrected with this procedure. The non-working part of the Module 0 leads to an overestimation of the RMS. However, the effect can be estimated by the MC simulation and is found to be negligible. The biggest effect is observed at the highest energy where it reaches 0.1%.

The beam energy has been precisely determined for each run using the measured currents in the bending magnets and the collimator setting. The exact numbers together with the nominal beam energy are given in Tab. 2.

In this analysis, the raw cell energies as obtained from summing the two PMT signals (given in pC) are used to perform the measurements. No attempt is made to correct the energies for invisible energy losses during the hadronic shower development. The signal-to-energy conversion factor for electrons impinging from the side $e = 1.07$ pC/GeV defines the electromagnetic energy scale for data taken in this set-up [7] and is used to compare data to simulations. However, in most of our results this factor cancels out.

The basic calibration of the TileCal cells has been checked using electrons and muons. The electron signal is defined as the sum of the first and the second cell that are hit by the impinging beam. The electron response normalized to the beam energy for electron between 20 to 180 GeV has been found to be linear within 1% using several different data sets.

The electrons allow to check the calibration of the first cell which contains about 90% of electron total energy. If the deviation of mean total electron energy from the beam energy after application of electromagnetic energy scale factor e was larger than 1%, then a correction is applied to the first (edge) cell to get the beam energy correctly. In addition, electrons of the same energy, but impinging the calorimeter from the opposite side are used to validate this energy correction for the edge cell.

Only one cell was found where such a correction was necessary. This cell is one of the edge cells where the cell response equalization procedure using the photons emitted by a Cs-source shows problems. The calibration using the electron beam is therefore more reliable. By comparing the results of the Cs-calibration to the response of muons it can be concluded that a similar correction is not needed for all other cells

To further test also the calibration of the other cells of the TileCal the muon response normalized to the transversed path length per cell has been measured. The cells give the same response within 5 %.

4.2 Mean Energy Response and Energy Resolution

The measured mean total energy, normalized to the beam energy is referred to here as the response of the calorimeter. It is shown for pions and protons in Fig. 6. For pions, the response increases by about 7% from 20 to 180 GeV. The increase for protons is steeper.

Fig. 7 shows that for all energies the response is larger for pions, and that the ratio of the pion to proton response decreases towards higher energies. These results are in agreement with the previous measurements using prototype modules of the TileCal at projective angles [8].

The resolution defined as the root mean square divided by the mean energy (RMS/E) shown in Fig. 8 is about the same for pions and protons at low energies and is better for protons at higher energies ($E \geq 100$ GeV). The curve in the figure is the result of a fit of the pion resolution to the following parameterisation:

$$\frac{RMS}{E} = \frac{a}{\sqrt{E}} \oplus b, \tag{2}$$

which yields to $a = 49.4 \pm 0.3\%$ GeV$^{-1/2}$ and $b = 4.58 \pm 0.06\%$ and where E is the measured energy.

All these results (mean and RMS) are not biased by the cut on the average energy density. They stay stable within 0.2% when the cut on the energy density is removed in the MC simulation. The results of both means and resolutions are corrected for the measured beam contamination.

All these measurements reflect qualitatively the non-compensating nature of the TileCal that leads to a different response to the hadronic and electromagnetic energy depositions during the shower development. They are, moreover, consistent with a larger electromagnetic energy fraction in pion induced showers.

The different response of the TileCal to the electromagnetic and hadronic shower components is also clearly illustrated in Fig. 9, where the energy distribution normalized to the mean energy $\langle E_{tot} \rangle$ is compared for pions and protons at 100 GeV. The shapes are fitted by a Gaussian in the region between $0.8 < E_{tot}/\langle E_{tot} \rangle < 1$ and extrapolated to the region $1 < E_{tot}/\langle E_{tot} \rangle < 1.2$, where the energy response is larger than the mean and more events are seen than would be expected, if the whole energy distribution was Gaussian. In this region the electromagnetic energy fractions appears to be higher.

The bias introduced by the particle identification cuts are smaller than 2 % up to values around 1.1 and then increases up to 10 % towards the end of the ratio.

The clear asymmetry between low and high energy depositions is even more visible in the ratio of the data to the extrapolated Gaussian fit[15] shown in Fig. 10. In the region $E_{tot}/\langle E_{tot} \rangle < 1$, where the energy is lower than the mean, the measured shape is compatible with a Gaussian. In the region above the mean, for both pions and protons, an increasingly larger number of events is seen in the measured distribution. This effect is more pronounced for pions than for protons. This nicely illustrates the different pion and proton responses in the calorimeter: protons have a more symmetrical shape with a less pronounced left-right asymmetry than pions, as a consequence of the larger size and of larger fluctuations in the electromagnetic content of pion induced showers.

[15] To obtain the ratio, the integral of the fitted Gaussian is calculated for each bin, divided by the bin width and by the number of data events in this bin.

In previous analyses, the mean energy responses of pions and protons were determined as the peak of a Gaussian fit within $\pm 2\sigma$ using the standard projective geometry of TileCal [8, 9]. In the set-up used in these analyses Barrel Module 0 was located in the center surrounded by 5 prototype modules. In such a geometry the shower is not fully contained. The presence of longitudinal leakage in these data resulted in large tails on the energy distribution and an energy resolution that was worse by approximately 10-20 % has been measured. However, the ratio of the mean energy responses of protons and of pions (which is less affected by leakage) is compatible with the result presented here.

4.3 Longitudinal Shower Profiles

The measured longitudinal shower profiles for pions and protons are presented in Fig. 11. The normalisation is done with respect to the mean total measured energy. The depth of the layer is taken to be the size of the B sub-cell, since most of the energy is deposited here. In this section the longitudinal profile are not corrected for the effect of the projective form of the BC cells, the shift of the A cell with respect to the B sub-cell[16]. Such corrections will be discussed and applied in Section 5.3.

The measurements extend up to 20 λ in depth. On average, both types of hadron showers quickly deposit their energy and reach the point within the first few λ in depth where the mean energy deposition is maximal. The average energy deposition then exponentially decreases towards the end of the shower and is down by approximately four orders of magnitudes at 15 λ.

The long tail at the end of the shower becomes flatter, when the mean energy loss per cell is compatible to the noise fluctuations. The measurement is stopped at this depth.

For pions and protons the shape of the average longitudinal profile is shown in Fig. 11 for different energies. The showers penetrate deeper with increasing hadron energy.

The ratio of the profiles of showers induced by pions and protons is presented in Fig. 12. Since the statistical uncertainties of the measured longitudinal profiles are relatively higher at the end of showers, the ratios are only presented for a limited range of depth that depends on the energy. At 50 GeV the pion to proton ratio is flat and close to 1, up to a depth of 10 λ. It decreases with depth at higher energies.

This behavior may be explained by the higher proton interaction cross-section with iron nuclei. Therefore, pions, on average, penetrate deeper in the calorimeter. This results in fewer hadronic interactions initiated by pions in the first one or two cells, which, however, are characterized by a higher fraction

[16]The cells are grouped as follows: B9 and A10, BC8 and A9, BC7 and A8, BC6 and A7, BC5 and A6 and A5, BC4 and A4, BC3 and A3, BC2 and A2, BC1 and A1.

of neutral pion production by pions. These two differences in the underlying mechanism of shower development for pions and protons have opposite effects on longitudinal profiles and happen to balance out at 50 GeV.

The bias resulting from the electron rejection cut (see Section 3.4) on the pion and proton longitudinal shower profile can be evaluated by using the results of simulations with different hadronic interaction models where electron and pions or protons are mixed together according to the measured beam composition and by comparing the results with and without the electron rejection cuts. A systematic uncertainty of maximally 4% is found on the measured value in the first layer using QGSP physics list. As will be shown later, QGSP predicts too short and too narrow hadronic showers and the systematic uncertainty is therefore overestimated. Using the LHEP_BERT physics list only a bias of 1% was found on the same quantity.

Since the normalisation of the longitudinal profile is chosen to be the total energy, also other layers can be affected. However, the bias due to the electron rejection cut is at least 2 times smaller. The systematic uncertainty introduced by the muon identification cut can be evaluated by looking at the observables with and without the cut on the discriminant (see Section 3.4) as well as using the results of simulation. The resulting systematic uncertainty is found to be smaller than the statistical uncertainty.

4.4 Lateral Spread

In Fig. 13 the ratio of the energy deposit in the Module 0 and in the production Barrel Module is presented. The distance of the beam impact point in the Barrel Module to the Module 0 is 0.6 λ. The ratio is a simple estimator of the lateral spread of the shower. Since the measured ratio is larger for pions than for protons, pion induced showers are laterally narrower. This may come as surprise, since pion showers have just been shown to be longer.

This observation might be qualitatively explained by the difference in the electromagnetic energy contents of pion and proton showers. Most of the energy is produced near the core of the shower. Since electromagnetic showers are compact, the electromagnetic energy is deposited relatively close to the core of the shower. Assuming that the hadronic energy deposited in the pion and the proton showers has the same lateral spread, the above defined ratio will be as much different as the inverse ratio of the electromagnetic energy fraction. Since the electromagnetic energy fraction is larger by about 20 % (see Section 3.3), the 20% larger lateral spread for protons is consistent with this interpretation.

4.5 Comparisons to Monte Carlo Simulations

The simulated responses obtained for pions and for protons when either physics lists included the Bertini cascade model are in better agreement with the data than found with LHEP and QGSP. This is shown in Fig. 14 where both data and MC are first normalized to the electromagnetic scale and then the ratio between MC and data is shown. For the MC the electromagnetic energy scale is obtained using the results of electron simulations. The normalisation is chosen such that the mean electron energy in MC equals to the beam energy. The QGSP_BERT physics list describes the absolute pion response within 1 % (2 %) for pions (protons), while for QGSP the pion (proton) response is 4% at high energy (8% at low energy) lower in the MC.

For both MC simulation models LHEP and QGSP, the RMS spread is larger by about $10 - 20$ % in the MC than found in the data. Adding the Bertini cascade brings the simulation in better agreement with the data (within 5 % for pions and 10 % for protons). This is shown in in Fig. 15. Taking into account the good description of the mean total energy and the RMS spread by the Bertini models, in particular, by QGSP_BERT, we conclude that adding the Bertini cascade model leads to a good description of TileCal energy resolution.

In Fig. 16 the measured pion shower profiles are compared to all physics lists for all energies. To make the direct comparison easier, the ratio of the simulated shower profiles to the ones measured in the data are shown in Fig. 17. The predictions of the hadronic physics lists vary significantly.

The LHEP physics list describes the data above 50 GeV quite well, i.e. within 10% for the first 10 λ. At low energies the simulated showers are, however, too short. The QGSP physics list predicts too short showers over the full energy range. Approximately 50% less energy is predicted at a depth of 10 λ as compared to the data[17].

Adding the Bertini inter-nuclear cascade model makes showers longer in both physics lists, LHEP and QGSP. This is probably due to the larger number of low energy neutrons produced by this model. For the LHEP physics list above 50 GeV the showers are too long. In the case of the QGSP physics list, adding the Bertini cascade leads to noticeable improvements in the description of the data. In the first 10 λ the data are reproduced within a precision of $\pm 20\%$. At 10 λ LHEP_BERT is 20 % too high, while QGSP_BERT is 20 % too low. Unlike LHEP, in case of the QGSP list (with or without Bertini's model) the underestimation of the longitudinal shower profiles is consistent in the energy range 20 to 180 GeV.

For proton shower profiles shown in Fig. 18 similar conclusions can be drawn. As shown in Fig. 19, the LHEP physics list describes the data quite well above

[17]Note, that for 20 GeV energy almost the same model (LEP) is used for both physics lists, QGSP and LHEP.

50 GeV, while QGSP predicts too short showers in the full energy range. Using the Bertini model in addition makes shower longer and a better agreement to the data is observed.

The description of the data for protons is in general worse than the one for the pions for all physics lists.

The ratio of energy deposition in the Barrel and Module 0 for data and simulation is presented in Fig. 20. Both physics lists, QGSP and LHEP, predict showers with a lateral spread significantly narrower than the one measured in the data for both pions and protons. The description of QGSP is worse than the one of LHEP. Adding the Bertini cascade leads to a good description of the data for both physics lists. LHEP_BERT gives the best description.

In conclusion, QGSP predicts showers that are too short and too narrow. LHEP reproduces the longitudinal shower shape correctly for $E > 50$ GeV, but the showers are too narrow. Adding the Bertini cascade model makes showers longer and wider. For QGSP this reproduces the data better, while for LHEP the description of the longitudinal shower profile becomes worse.

The physics lists QGSP and LHEP, together with the Bertini cascade model were therefore used to evaluate the electron contamination in the pion sample and to estimate the systematic uncertainty introduced by the cut on the average energy density (see Section 3.4).

5 Phenomenological Interpretation

5.1 Electromagnetic Content in Pion and Proton Induced Showers

In the previous sections it has been shown that the various measurements can be consistently interpreted, if pion showers have a larger electromagnetic energy fraction than proton induced ones. For a more quantitative analysis the phenomenological model of ref. [1] is used[18].

The energy response (on the electromagnetic energy scale) divided by the beam energy E_{beam} can be written as:

$$R = \frac{E}{eE_{beam}} = f_{em}^{p/\pi} + \frac{h}{e}(1 - f_{em}^{p/\pi}) \tag{3}$$

where e (h) is the calorimeter response efficiency to the electromagnetic (hadronic) energy (alternatively, signal-to-energy conversion factor for the electromagnetic (hadronic) components of the shower) and $f_{em}^{p/\pi}$ is the electromag-

[18] Another phenomenological model parameterizing the energy behavior of hadrons sometimes used in calorimeter studies, was proposed by Fabjan et al., [14] and used by Wigmans [15]. The parameterisation of ref. [1] has the advantage that the electromagnetic energy fraction at very high energy has the correct limit, therefore it is used in this analysis.

E_{beam}^{nom} [GeV]	20	50	100	180
E_{beam}^{meas} [GeV]	20.21	50.36	100.54	179.73
$\langle E_\pi \rangle / E_{beam}^{meas}$	0.8101 ± 0.0007	0.8436 ± 0.0009	0.8514 ± 0.0005	0.8676 ± 0.0006
$\langle E_p \rangle / E_{beam}^{meas}$	$--$	0.8111 ± 0.001	0.8258 ± 0.0003	0.8476 ± 0.0004
A_π [%]	99.27	99.33	99.34	99.42
A_p [%]	$--$	99.20	99.29	99.33
$(RMS/\langle E \rangle)_\pi$ [%]	11.92 ± 0.06	8.78 ± 0.08	6.51 ± 0.04	6.02 ± 0.05
$(RMS/\langle E \rangle)_p$ [%]	$--$	8.5 ± 0.1	5.80 ± 0.03	5.09 ± 0.03
$\langle E_\pi \rangle / \langle E_p \rangle$	$--$	1.040 ± 0.002	1.0311 ± 0.0008	1.0236 ± 0.0008

Table 2: The nominal and measured beam energy, the mean measured response corrected for lateral leakage and contamination, the estimated lateral containment ($A_{\pi/p}$) and the relative resolution (root mean square divided by mean of the measured energy distribution) for pions and protons. The pion to proton ratio is also given. Only statistical uncertainties are quoted.

netic energy fraction for proton and pion induced showers that is parameterised according to ref. [1]:

$$f_{em}^{p/\pi}(E) = 1 - \left(E/E_0^{p/\pi}\right)^{m-1} \tag{4}$$

where m and $E_0^{p/\pi}$ are free parameters. The range of these parameters is obtained in ref. [1] using a MC simulation for iron. The parameter $E_0^{p/\pi}$ is the extrapolated energy at which the cascade is entirely hadronic, or an effective turn-on energy for π^0 production. The power m is expected to be the same for pions and protons [1]. This parameterisation is in agreement with various measurements.

The fit is based on the data summarized in Table 2.

The data are corrected for lateral containment that can be estimated using runs where the beam hits the tile 5 in the Extended Barrel module. Assuming that the lateral shower development is symmetric around the axis of the impinging particle, the lateral energy leakage can be determined from the energy deposition in Module 0 and therefore the lateral energy leakage in case when the beam hits the center of barrel module can be determined.

The lateral containment thus determined for pions (A_π) and protons (A_p) is also given in Table 2.

The energy response is fitted to the data using eq. 3 only by fixing the electromagnetic energy scale parameter $e = 1.07$ pC/GeV and the pion extrapolated energy parameter $E_0^\pi = 1$ GeV. Following the arguments in ref. [1], we also assumed that the exponents for pions (m^π) and for protons (m^p) are equal. In this way only three free fit parameters are left, the ratio (e/h), the proton extrapolated energy parameter E_0^p and the exponent m.

The fit is done simultaneously on the pion and proton data.

The result of the fit is shown in Fig. 21. The fit describes the response to pions and protons well assuming a point-to point systematic uncertainty of 1%.

The e/h ratio is found to be $e/h = 1.44 \pm 0.07$, the parameter $E_0^p = 2.71 \pm 0.68$ GeV and the exponent $m = 0.84 \pm 0.03$ [19].

The extracted ratio of the electromagnetic fraction for the pion and proton induced showers is shown in Fig. 22 as a function of the beam energy. The light band indicates the uncertainty due to the uncertainties on the fit parameters.

The electromagnetic energy fraction in proton induced showers is about 3/4 of the value of that fraction for pion showers. The ratio rises towards higher energies. This is in contrast to the ratio of the hadronic energy fraction of pions and protons which is a constant for different energies as shown in Fig. 22 (dark band)[20].

5.2 Analytical Description of Longitudinal Profile

Bock et al. [18] suggested the following parameterization for the hadronic shower longitudinal profile in analogy to the formula describing the longitudinal electromagnetic shower profile [19]:

$$\frac{dE_s}{dx} = N\left\{ w\left(x/X_0\right)^{a-1} e^{-bx/X_0} + (1-w)\left(\frac{x}{\lambda}\right)^{a-1} e^{-d\frac{x}{\lambda}} \right\}, \qquad (5)$$

where N is a normalization constant, a, b, d, w are free parameters, λ is the nuclear interaction length, X_0 is the radiation length[21] and x is the distance from the shower vertex. According to the authors the first (second) term describes electromagnetic (hadronic) shower component.

Even with the segmentation of the TileCal used in non-projective geometry, an accurate determination of the shower vertex position (shower start) is not possible. Therefore, eq. (5) needs to be convoluted with $\exp(-x/\lambda)$, which is the probability for a hadron to pass the distance x without undergoing a hadronic (inelastic) interaction [18]:

$$\frac{dE}{dx} = \int_0^x \frac{dE_s(x-x_v)}{dx} e^{-x_v/\lambda}\, dx_v\,, \qquad (6)$$

[19] When assuming only statistical uncertainties, the fit parameters are: $e/h = 1.42 \pm 0.01$, $E_0^p = 2.67 \pm 0.04$ GeV, $m = 0.83 \pm 0.002$. For completeness, we also give the parameter obtained for the parameterisation [14, 15] $f_{em}^{p/\pi} = k^{p/\pi} \log\left(E/E_0^{p/\pi}\right)$, where we set $E_0^\pi = 1$ GeV. The results are: $k^p = k^\pi = 0.1 \pm 0.01$, $e/h = 1.36 \pm 0.03$, $E_0^p = 2.65 \pm 0.65$ GeV.

[20] The constant hadronic energy fraction is a consequence of the assumption that the exponents m for pion and protons are equal. However, we have checked that without this assumption m^π and m^p are equal within the uncertainties and the other fit parameters are also within the quoted uncertainties.

[21] We use throughout this analysis an effective radiation length for the Tile calorimeter $X_0 = 2.24$ cm.

where x_v is the coordinate of the shower vertex. The calculation of the above integral results in [20]:

$$\frac{dE}{dx} = N\left\{ \frac{wX_0}{a}\left(\frac{x}{X_0}\right)^a e^{-bx/X_0}\,{}_1F_1(1,1+a,(b-\frac{X_0}{\lambda})\frac{x}{X_0})+ \right. \\ \left. \frac{(1-w)\lambda}{a}\left(\frac{x}{\lambda}\right)^a e^{-dx/\lambda}\,{}_1F_1(1,1+a,(d-1)\frac{x}{\lambda})\right\}, \tag{7}$$

where ${}_1F_1(a,b,c)$ is the confluent hyper-geometric function [21], which can be calculated using the GNU scientific library.

The normalization constant is obtained requiring:

$$\int_0^\infty \frac{dE}{dx}\,dx = E_{beam} \tag{8}$$

which gives

$$N = \frac{E_{beam}}{\lambda\Gamma(a)(wX_0 b^{-a} + (1-w)\lambda d^{-a})}, \tag{9}$$

where $\Gamma(a)$ is the Gamma function[22]. To describe the normalized shower profile in eq. 8 and eq. 9, E_{beam} has to be replaced by 1.

5.3 Unfolding the Longitudinal Profile

The cell geometry of TileCal was optimized for the measurement of particles coming from the LHC interaction point. For particles penetrating from the side, as analyzed here, the cells of the same layer are shifted relative to each other (see Fig. 1).

In particular, the second sampling (BC) of the TileCal consists of two relatively shifted sub-cells (B and C). The shift varies with the depth decreasing in the middle and increasing in opposite directions towards the end. The beam hits the center of the B sub-cell which is about 2 λ thicker and the main energy deposition occurs here.

The shower profiles presented in Fig. 11, Fig. 16 and Fig. 18 do not include any correction for the projective form of the BC cells and the contribution from the relative shift of the A cells with respect to the B sub-cells of the same layer. This creates a bias, since it is assumed that all the energy is deposited within the granularity (the segmentation along the shower axis) given by the B sub-cell.

The unfolding procedure described below is designed to transform the data set of responses obtained for the projective cell geometry to the data of non-projective configuration defined as the energy deposit in the consecutive calorimeter layers with locations and thicknesses coincident with the ones of the B sub-cells. This is possible to realize using the parameterization of the longitudinal profile of the A sampling and of the lateral shower profile at different depths. In

[22] We have corrected an error in the normalisation constant in [20].

addition, we correct the measured longitudinal energy profiles for lateral leakage that has been determined from data for each depth.

As a first step of the unfolding, the contribution of the C sub-cells into the BC cell response has to be determined. The distances from the shower axis to the A and C samplings are equal, but the C cells are larger in the transverse dimensions (as well as longer) and therefore for the estimation of their content the knowledge of the lateral shower profile at each given depth is necessary.

The longitudinally integrated lateral shower profile of pions in a lead-scintillator calorimeter [22] can be described by the following function:

$$\frac{dE}{dr} = \frac{G_1}{r} e^{-\frac{r}{\lambda_1}} + \frac{G_2}{r} e^{-\frac{r^2}{{\lambda_2}^2}}, \tag{10}$$

where G_1, G_2, λ_1 and λ_2 are free parameters. The central core of the shower described by the second term of eq. 10 (with a typical value of $\lambda_2 = 3.8$ cm) is mainly attributed to the compact electromagnetic energy contribution in hadron showers, while the first term describes the mostly hadronic tail with a typical value of $\lambda_1 = 14.3$ cm. It is interesting to note that similar values of parameters have been obtained in this analysis of TileCal data when fitting the longitudinally integrated energy depositions of the A, BC and D cells of the Barrel Module and the Module 0. However, for the unfolding procedure applied here, a different fit was done.

The transverse dimensions of the B sub-cells are much larger than the typical value of the λ_2 parameter and thus the contribution of the second term of eq. 10 to the response of the A cell and C sub-cells is negligible. Since the lateral width of the hadronic shower changes with depth, the differential description of the lateral profile by eq. 10 at the given depth correspondingly requires a change in the value of λ_1. The measurements in ref. [22] were integrated over the depth.

The ratio of the response of the A cells of the Module 0 to those of the production Barrel Module for a given energy can be fit to as a function of only a depth dependent λ_1 parameter. As an example, this ratio is shown in Fig. 23 for 50 GeV pions. It was fit, for all beam energies available, using the first term of eq. 10 and assuming a quadratical shower depth dependence of the λ_1 parameter.

The extracted λ_1 is 14.3 cm at the beginning of the shower and slowly reaches a minimum of 12.3 cm at a depth of 3λ. After that, it increases approximately quadratically up to 30 cm at 10λ. These results are close to the ones obtained in ref. [22] for the lead-scintillator calorimeter SPACAL, despite of the difference in the corresponding absorber media of the two calorimeters. In case of an iron absorber the ratio of the number of neutrons to protons in the nucleus N/Z is 1.15, while for lead it is approximately 30% larger. This difference might give rise to a higher neutron activity in the lateral profile due to more energy flow through neutron evaporation and spallation processes, having relatively

isotopic angular distributions (see ref. [23]), and therefore, a different lateral profile might be expected.

From the dependence of the radial attenuation length λ_1 on the shower depth, the ratio of the energy depositions in C and A cells at a given depth can be determined.

In the Barrel Module it was found that at the beginning of the shower the ratio of the energy in the C sub-cell to that in the A cells is about 1.4, whereas at the end of the shower, around a depth of 20 λ, the ratio is about 1.6, with a weak dependence on beam energy. In Module 0, the C/A ratio is about 1.3 at the beginning of the shower, and reaches about 1.5 at about 20 λ.

Using the knowledge of radial attenuation length, a procedure to correct for the bias introduced by the projective cell geometry has been developed that rearranges the energy measured in the projective BC cells to the B and C sub-cells. This correction procedure is as follows:

1. a fit to the longitudinal profile of the sampling A, using eq. 7 is performed[23] The fit results and the corresponding data are shown in. Fig. 24;

2. the integrals of the longitudinal profile for the cell boundaries of the C sub-cell is calculated. This corresponds to the energy the C sub-cell would have, if it had laterally the same dimensions as the A cell;

3. using the known ratio of the energy depositions in the C and A cells the contribution of C sub-cell is calculated;

4. the energy in the B sub-cell is calculated from the calculated energy in the C sub-cell and the measured energy in the BC cell.

5. At this point, we calculate the energies in the "virtual" A cells and C sub-cells defined to have the same longitudinal boundaries as the B sub-cells, in both the production module and in Module 0. Care is taken that the integrals over the total depth of the A and C cells are preserved.

6. the energies of the "virtual" A and C cells and of "real" B sub-cells are added

The developed algorithm corrects for all effects coming from cell geometry and the resulting shower profile is the one that would be measured, if the calorimeter modules had towers of non-projective form.

The corrections change the shower profile only by less than 5% in the region where the shower is broad and the relative shift of the B and the C sub-cells is largest.

As an example in Fig. 24 the profile of BC and A samplings of Barrel module is presented for 100 GeV pions. The line is the result of the fit of the shower

[23]Here, only the second term in eq. 7 is used.

profile using the second term of eq. (7) in the A sampling which is used in the unfolding procedure. Here, the total energy E deposited in the given sampling is also assumed to be a free parameter on which the normalisation factor N depends as in eq. 9. The following values of parameters have been obtained:

$$a = 2.311, \;\; d = 0.608, \;\; E = 0.842. \tag{11}$$

The energy deposition in the BC sampling is fit using eq. (7) leaving E to be a free parameter. From the fit the following values of parameters are obtained:

$$a = 1.932, \;\; b = 0.199, \;\; d = 0.688, \;\; w = 0.341, \;\; E = 84.04. \tag{12}$$

In the beginning of the shower the contribution of the A sampling is two orders of magnitude smaller than one of the BC sampling, but its relative importance increases with the shower depth. Taking into account that the energy deposition in the C sampling is larger than energy deposition in the sampling A by only 40% , one clearly sees that the energy in the B sampling is the main contribution at the chosen geometry. Towards increasing shower depth the contribution of the B sampling decreases. The relative shift of the B and C sub-cells is large at the beginning of the shower, reaching at most the shift between two neighboring A cells. The difference of energy depositions in the neighboring A cells multiplied by the C/A ratio, is, in the worst case, a few percent only as one can see from the Fig. 24.

In addition, the longitudinal shower profiles are corrected for lateral leakage. The correction was obtained using runs where the beam hits into tile 5 of the Extended Barrel module and the shower profile was measured in Module 0. The displacement of the Extended Barrel module with respect to the Barrel one is taken into account. The measured profile was added to the main measurements. The effect of lateral leakage increases with the depth almost linearly reaching a level of 3% at 15 λ.

The corrected pion and proton shower profiles are shown in Fig. 25, Fig. 26 and Fig. 27. The profiles are also given in Tables 3 and 4.

5.4 Adjustment of the Analytical Longitudinal Shower Shape Parameterisation to the Unfolded Data

In order to fit the experimental data using eq. 7 simultaneously for the various energies, the parameters a and w are assumed to have a logarithmic energy dependence, while b and d are assumed to be energy independent. This energy behavior of the free parameters makes it possible to fit simultaneously all available data.

x	20 GeV	50 GeV	100 GeV	180 GeV
1.67	0.240 ± 0.001	0.207 ± 0.002	0.164 ± 0.002	0.152 ± 0.002
3.45	0.214 ± 0.001	0.208 ± 0.002	0.211 ± 0.002	0.211 ± 0.002
5.09	0.0921 ± 0.0006	0.107 ± 0.001	0.121 ± 0.001	0.121 ± 0.001
6.69	0.0366 ± 0.0003	0.0491 ± 0.0008	0.0582 ± 0.0008	0.0626 ± 0.0007
8.15	0.0154 ± 0.0002	0.0217 ± 0.0004	0.0295 ± 0.0005	0.0331 ± 0.0004
9.61	0.0059 ± 0.0001	0.0096 ± 0.0003	0.0141 ± 0.0004	0.0156 ± 0.0003
10.99	0.00187 ± 0.00006	0.0037 ± 0.0002	0.0062 ± 0.0002	0.0073 ± 0.0003
12.37	0.00080 ± 0.00004	0.0018 ± 0.0001	0.0030 ± 0.0001	0.0036 ± 0.0001
13.74	0.00045 ± 0.00002	0.00079 ± 0.00009	0.0014 ± 0.0001	0.00165 ± 0.00007
15.12	0.00012 ± 0.00002	0.00030 ± 0.00005	0.00056 ± 0.00007	0.00079 ± 0.00004
16.49	$--$	0.00017 ± 0.00004	0.00023 ± 0.00005	0.00040 ± 0.00005
17.87	$--$	0.00006 ± 0.00002	0.00015 ± 0.00005	0.00019 ± 0.00002
19.33	$--$	$--$	$--$	0.00007 ± 0.00001
20.80	$--$	$--$	$--$	0.00004 ± 0.00001

Table 3: Pion longitudinal shower profile for different beam energies. The values given in the first column correspond to the upper edge of the bins. The first bin starts at a depth of 0.12 λ corresponding to the depth of the end plate of the TileCal. Only statistical errors are given.

x	50 GeV	100 GeV	180 GeV
1.67	0.204 ± 0.003	0.185 ± 0.002	0.167 ± 0.002
3.45	0.209 ± 0.003	0.214 ± 0.002	0.212 ± 0.002
5.09	0.107 ± 0.001	0.1150 ± 0.0009	0.119 ± 0.001
6.69	0.0494 ± 0.0009	0.0521 ± 0.0005	0.0594 ± 0.0006
8.15	0.0221 ± 0.0005	0.0243 ± 0.0003	0.0288 ± 0.0003
9.61	0.0096 ± 0.0003	0.0106 ± 0.0002	0.0129 ± 0.0002
10.99	0.0038 ± 0.0002	0.0043 ± 0.0001	0.0056 ± 0.0001
12.37	0.0014 ± 0.0001	0.00191 ± 0.00006	0.00249 ± 0.00007
13.74	0.00049 ± 0.00006	0.00078 ± 0.00003	0.00116 ± 0.00005
15.12	0.00012 ± 0.00003	0.00031 ± 0.00002	0.00050 ± 0.00002
16.49	0.00007 ± 0.00002	0.00011 ± 0.00001	0.00013 ± 0.00002
17.87	0.00002 ± 0.00001	0.00002 ± 0.00001	0.00006 ± 0.00001
19.33	$--$	$--$	0.00002 ± 0.00001
20.80	$--$	$--$	$--$

Table 4: Proton longitudinal shower profile for different energies. The values given in the first column correspond to the upper edge of the bins. Only statistical errors are given.

The curves in Figs. 25, 26, 27 represent the results of the fit obtained for pions and protons. The following parameter values have been obtained for pions:

$$a = -0.084 + 0.532 \ln E_{tot}(\mathrm{GeV}), \quad w = 0.675 - 0.0696 \ln E_{tot}(\mathrm{GeV}), \tag{13}$$

$$b = 0.249, \quad d = 0.751, \tag{14}$$

and for protons:

$$a = 0.886 + 0.279 \ln E_{tot}(\mathrm{GeV}), \quad w = 0.693 - 0.0699 \ln E_{tot}(\mathrm{GeV}), \tag{15}$$

$$b = 0.257, \quad d = 0.767. \tag{16}$$

The parameter E_{tot} denotes the total energy in the calorimeter.

The parameterised profile was integrated over the depth of each cell and the integrals were fitted to the experimental points. With this procedure the parameterisation is independent of the geometry of the calorimeter cells. The parameterisation obtained describes the experimental data within $5 - 10\%$ for pion and protons.

The obtained values allow to calculate analytically the energy deposition at each given depth of the calorimeter for pions and protons within the energy range of 20 to 180 GeV. For higher energies the empirically found energy dependence of the parameters might be useful. The longitudinal shower profile of pions and protons is also presented in Tab. 3 and Tab. 4.

5.5 Comparison of TileCal Data to Previous Measurements

The pion longitudinal shower profiles obtained in Section 5.3 can be compared with previous measurements made in the energy range of $10 - 140$ GeV using the iron-scintillator CDHS calorimeter [3].

The CDHS calorimeter has a finer granularity than TileCal, but only a depth of 12.4 λ, which is more than twice as short as TileCal's special set-up used in this work. The iron-scintillator volume ratio of CDHS calorimeter is similar to one of TileCal, but it has a sampling frequency that is approximately 2 times smaller. In order to compare with our results, the effective nuclear interaction length of the CDHS calorimeter ($\lambda = 19.5$ cm[24]) is used to change the units of the abscissa of the data presented in ref. [3].

The comparison of TileCal and CDHS pions shower profiles for beam energies of 20, 50 and 100 GeV is presented in Fig. 28. The superimposed curves are the results of the fit to the TileCal data presented in Section 5.4. In ref. [3] no possible contamination of the pion beam by proton is mentioned.

[24]The effective nuclear interaction length of the CDHS calorimeter is calculated using the known fraction of material used in the detector construction and their nuclear interaction lengths.

Good agreement between the TileCal data and more finely sampled data of the CDHS calorimeter is observed. The parameterisation obtained using TileCal data describes the CDHS shower profiles within an accuracy of 10%. It is remarkable that the shower profiles measured in ref. [3] for beam energies (10, 15, 30, 75, 120 and 140 GeV), which were not available in our data set, are also described with the same accuracy by the analytical parameterisation. This shows that the determined energy dependence of the fit parameters is correct.

From the analytical function and the parameters given in ref. [3] we were not able to reproduce the shown shower profiles and therefore we can not overlay this parameterisation and compare with the one obtained in this work.

For 100 GeV pions the longitudinal shower profile was measured in ref. [4] using TileCal prototype modules for particles impinging the detector at 10 degrees. For the construction of the TileCal prototype modules the same materials with the same relative fraction were used as for production modules, therefore both have the same nuclear interaction length. The energy deposition values in different samplings presented in Tab. 4 of ref. [4] are used. The comparison of shower profiles obtained with TileCal prototype modules with the one obtained in this work is presented in Fig. 29. The shower profile measured with prototypes are normalized such that the area below the profile equals 1. The parameterisation obtained in this work as well as the measurement are also normalized in the same way using as a scale factor integral of the parameterisation within the range corresponding to the prototype measurements. In order to be able to compare the old measurement with the parameterisation easily, the integral of the shower profile is calculated within each bin of the prototype measurement and divided by the bin width. The old measurement is described with 10% accuracy.

In ref. [4] a negative pion beam has been used. The proton contamination was therefore negligible.

The successful comparison of the parameterisation obtained in this work with a parameterisation of earlier TileCal data presented in ref. [20] is impossible, because it is not reproducible from the information given in ref. [3] and ref. [20].

6 Influence of Longitudinal Shower Fluctuations on the Energy Measurement

6.1 Evaluation of the Dependence of the Mean and the "Peak" on the Calorimeter Depth

The analytical parameterization of the longitudinal shower profile (see Section 5.3) allows to calculate the average longitudinal energy leakage for a given energy and a given depth. As an example, Fig. 30 shows the results of the

	pion		proton	
E_{beam} [GeV]	a [%]	b [cm]	a [%]	b [cm]
20	78.4	37.9	$--$	$--$
50	112	36.8	330	29.5
100	127	37.9	180	34.5
180	198	35.8	187	36.1

Table 5: The values of the parameters of the fit functions describing the peak leakage dependence on the calorimeter depth.

	pion		proton	
depth [cm]	a [%]	b	a [%]	b
135	0.774	0.341	0.871	0.311
165	0.360	0.322	0.289	0.362
195	0.173	0.315	0.052	0.540
223	0.128	0.211	0.020	0.566

Table 6: The values of the parameters of the fit functions describing the peak leakage dependence on the beam energy.

average longitudinal leakage calculations for TileCal production modules for a calorimeter length that corresponds to a pion or proton entering at $|\eta| = 0.35$ in projective geometry.

The average longitudinal leakage is roughly proportional to the logarithm of the beam energy. Above 50 GeV pions exhibit a larger leakage fraction than protons.

The η dependence of the average longitudinal energy leakage for 100 GeV pions and protons is presented in Fig. 31.

It is interesting to compare these results on the mean longitudinal energy leakage to the leakage defined with respect to the peak of a Gaussian fit to the total energy distribution within $\pm 2\sigma$. This peak leakage is more relevant, since most analyses quote the energy response with respect to a Gaussian fit and not with respect to the mean, i.e. tail effects are usually neglected.

The special test-beam set-up used in this analysis allows to measure the peak leakage with the granularity of a TileCal cell. The energy is measured by including all TileCal cells up to a certain depth and a Gaussian is fit to the resulting energy distribution. The leakage calculation based on these peaks are shown in Fig. 32 a) for pions and in Fig. 32 b) for protons as a function of the calorimeters length. The superimposed lines allow to interpolate between the measured points. The data have been fit with a function $a \times \exp(-x/b)$ and the parameters are given in Table 5. On top of Fig. 32 the pseudo-rapidity values (η) corresponding to a given depth of TileCal in the projective geometry are

also indicated. The energy dependence of the peak leakage based on the peak values is presented in Fig. 33 for various depths for pions and protons. The curves are the results of a fit with a function $a \times (E_{beam})^b$. The values of the parameters are given in Table 6.

As expected, the relative peak leakage decreased logarithmically with increasing depth and is relatively more important at high energies.

The peak leakage for a calorimeter length of 165 cm, corresponding to $\eta = 0.4$ in projective geometry for TileCal, is between $1-2$ % and it is similar for pions and protons.

6.2 Evaluation of the Dependence of the Energy Resolution on the calorimeter depth

The energy carried by particles escaping the calorimeter fluctuates event-by-event and deteriorates therefore the energy resolution. The longitudinal energy leakage has larger impact on the energy resolution than the lateral leakage (see ref. [23]), since the fluctuations of the longitudinal leakage are larger than those of the lateral leakage. This is because the longitudinal energy leakage strongly depends on the starting point of the shower, i.e. on the behavior of a single particle, the impinging one, while the lateral leakage is caused by a larger number of soft particles, each having small contributions to the total lateral leakage. In addition, the secondary products of most hadron-nucleus collisions are characterized with the exponentially decreasing spectrum of transverse energies, while the longitudinal energy spectrum of secondaries has large fluctuations. For 100 GeV pions 3.6 % average longitudinal leakage results in about 70 % worsening of the energy resolution (RMS/mean) of TileCal (see ref. [24]), while 6.6 % lateral leakage causes twice smaller degradation of the resolution.

Since in the test-beam set-up studied here, the calorimeter longitudinally fully contains the showers, the effect of the longitudinal leakage on the energy resolution can be quantified by shortening the volume, where the energy is reconstructed, in a controlled way. The dependence of the TileCal energy resolution on the depth of the calorimeter is studied by taking into account only signals from cells up to a certain depth.

Since the Barrel (Module 0) and Extended Barrel modules have different granularity, the response of the Module 0 cells is multiplied by a factor 2 to compensate the response of the Extended Barrel modules. Such a procedure guarantees the correct measurement of the mean energy, but leads to a systematic overestimation of the spread of the distributions. Below, the resulting bias is studied and the results are corrected for it.

For three depths, for which the measurements are presented later, it is possible to limit the depth of the Extended Barrel modules to be approximately equal to the chosen depth of the Barrel module and Module 0. This allows to

calculate the bias introduced on the spread of the energy distributions. The bias is determined for all beam energies and its weak depth dependence can be described by a first order polynomial function. It is about 10% both for RMS and σ at an energy of 20 GeV and decreases to 2% at an energy of 180 GeV. The following results are corrected for this bias.

The depth dependence of the TileCal energy resolution is shown in Fig. 34 for pions. In the upper plot the resolution is defined as the ratio of the RMS spread and the mean of the total energy distribution, while in the bottom one the resolution is defined as the ratio of the σ and the peak of a Gaussian fit to the total energy distribution in the range -2σ to 2σ around the peak value. With both definitions the resolution improves with increasing depth of TileCal. At a certain depth a further increase of the depth does not lead to an improved energy resolution. At low energies this point is reached at lower values of the depths than at high energies. The RMS/mean ratio changes more than the σ/peak one.

As an example in Fig. 35 the energy distribution of a pion with an energy of 100 GeV is shown for two depths of the calorimeter equal to 8 and 13.6λ. While for the larger depth, the energy distribution is approximately Gaussian, in the case of the smaller depth the longitudinal energy leakage results in a shift of the peak value and in large low energy tails in the energy distribution. This causes a relatively large increase of the RMS for shorter depths, while the σ is less sensitive to the low energy tails. This explains the different depth dependencies of the resolution defined in the two ways as mentioned above.

Summary and Conclusions

The response of the Tile calorimeter has been studied for pions and protons within the energy range of 20 to 180 GeV in a non-projective geometry where the hadronic shower is almost fully contained in the calorimeter.

The mean response of pions and protons slowly increases with beam energy, and the pion-to-protons response ratio is greater than one and slowly decreases with energy. The resolution is better for protons than for pions at higher energies. The total energy spectrum is not Gaussian, but is slightly skewed in the region where the measured event energy is larger than the average energy. This effect is larger for pions than for protons.

These observations are consistent with a higher electromagnetic energy fraction in the pion induced showers and larger fluctuations of this fraction. Expressing the energy dependence of the electromagnetic energy fraction of pion and protons showers as suggested in [1], it is found that this fraction for proton showers is about 75% of that of pion-induced showers. This ratio slowly increases with energy. The e/h ratio is found to be 1.44 ± 0.07.

The ratio of pion to proton electromagnetic energy fraction shows an energy dependence that is due to the stronger variation of the proton electromagnetic energy fraction. This is consistent with the worse resolution in the case of pions, and the negative slope of the energy dependence of the pion-to-protons energy ratio.

Longitudinal shower profiles have been measured up to a depth of 20 nuclear interaction lengths separately for pions and protons. The showers induced by protons are longitudinally shorter, but laterally wider. This can be explained by the larger inelastic cross-sections and by the lower fraction of electromagnetic energy depositions for protons.

The experimental data have been compared with the results of GEANT4 simulation, using two basic physics lists, LHEP and QGSP, as well as extensions where the Bertini intra-nuclear cascade is used. Neither of those physics lists is able to reproduce the data in the whole energy range satisfactorily, although the addition of the intra-nuclear cascade improves the description for QGSP. A simple estimator of the lateral shower spread of energies is well reproduced by Bertini's extension of both basic physics lists.

The longitudinal shower profiles unfolded for the non-projective cells configuration can be well fit with an previously derived analytical shower parameterization. This allows to calculate the energy deposition of pion and proton induced showers as a function of depth in the energy range up to 200 GeV.

The longitudinal shower profile of TileCal is in good agreement with the one from the iron-scintillator CDHS calorimeter.

The influence of longitudinal shower leakage on the energy resolution has been studied in the calorimeter configurations comprising less than the full containment length. The mean and the peak energy leakage as well as the degradation in the energy resolution for varying calorimeter depths have been determined for pions and protons.

Acknowledgments

We would like to thank all people that helped in the setting-up of the test-beam, in the data taking and in the data reconstruction and analysis. We would to thank in particular Alexander Solodkov, Tomas Davidek and Matteo Cavalli-Sforza for their continuous help and useful discussions. We grateful to our colleagues from the GEANT4 collaboration for their help with the MC simulation and many useful suggestions. We would thank our colleagues Y. Kulchitsky, L. Nodulman and S. Tokar for useful comments on the manuscript.

We would also thank INTAS for financial support as a PhD fellowship for M. Simonyan.

References

[1] T. A. Gabriel et al., Nucl. Instr. and Meth. A 338 (1994) 336; D. E. Groom, physics/0605164

[2] N. Akchurin et al., Nucl. Instr. and Meth. A 399 (1997) 202; N. Akchurin et al., Nucl. Instr. and Meth. A 408 (1998) 380.

[3] E. Hughes, Proc. 1st Int. Conf. on Calorimetry in HEP, FNAL, Batavia, 1990, p.525.

[4] P. Amaral et al., Nucl. Instr. and Meth. A 443 (2000) 51.

[5] S. Agostinelli et al., Nucl. Instr. and Meth. A 506 (2003) 250; version used GEANT4.7.1.patch01.atlas02.

[6] ATLAS collaboration, Tile Calorimeter Technical Design report, CERN/LHCC/96-42 ATLAS TDR 3, CERN.

[7] Testbeam studies of Production Modules of the ATLAS Tile Calorimeter, to be submitted to Nucl.Instr. and Meth.A.

[8] S. Constantinescu et al., ATLAS Internal note, ATL-TILECAL-2001-005.

[9] H. Hakopian, TileCal Analysis meeting presentation, TileCal-TIR-41, June 1998.

[10] H. S. Fesefeldt, Preprint: PITHA-85-02, Aachen (Germany) 1985.

[11] V. S. Barashenkov, P2-90-158 Dubna (Russia) 1990.

[12] H. P. Wellisch and D. Axen, Phys. Rev. C 54 (1996) 1329.

[13] M. P. Guthrie, R. G. Alsmiller and H. W. Bertini, Nucl. Instr. and Meth. 66 (1968) 29; H. W. Bertini and P. Guthrie, Nucl. Phys. A 169 (1971) 670; N. V. Stepanov, Preprint: ITEP-55 (Moscow) 1988.

[14] C. W. Fabjan and T. Ludlam, Ann. Rev. Nucl. Part. Sci. 32 (1982) 335.

[15] R. Wigmans, Nucl. Instr. and Meth. A 265 (1988) 273.

[16] M. Simonyan, ATLAS note, CERN-ATL-TILECAL-PUB-2006-003.

[17] F. Ariztizabal et al., Nucl. Instr. and Meth. A 349 (1994) 384.

[18] R. K. Bock et al., Nucl. Instr. and Meth. 186 (1981) 533.

[19] E. Longo and I. Sestili, Nucl. Instr. and Meth. 128 (1975) 283.

[20] Y. A. Kulchitsky and V. B. Vinogradov, Nucl. Instr. and Meth. A 413 (1998) 484.

[21] M. Abramovitz and I. A. Stegun, Handbook of Mathematical Functions, Columbia Univ. Press, New York (USA) 1964.

[22] D. Acosta et al., Nucl. Instr. and Meth. A 316 (1992) 184.

[23] R. Wigmans, Energy measurements in particle physics. Oxford University Press, 2000.

[24] M. Simonyan, PhD thesis.

[25] M. Hurwitz, ATLAS note, ATL-TILECAL-PUB-2006-008.

[26] Y. Kulchitsky et al., ATLAS note, ATL-TILECAL-PUB-2007-001.

[27] A. Solodkov and A. M. Henriques-Correia, presentation at the TileCal pion response task force meeting at 20.06.2007.

[28] L. Pribyl, Correlation between muon/Cs/electrons calibration, Presentation at the TileCal pion response task force meeting at 20.06.2007.

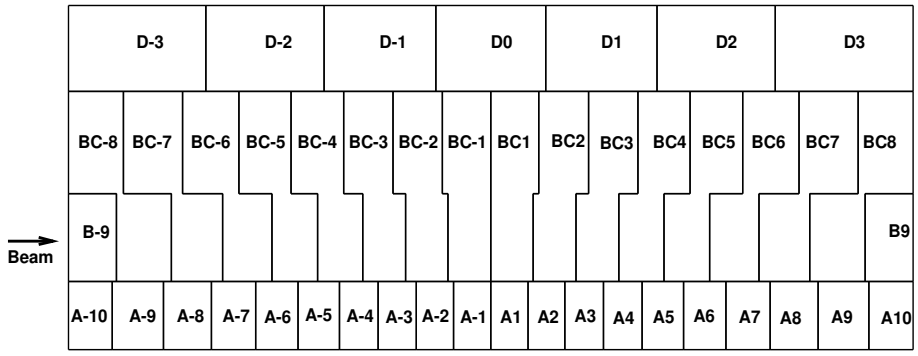

Figure 1: Scheme of the cell geometry of the barrel module and their impact on the Barrel Module under study.

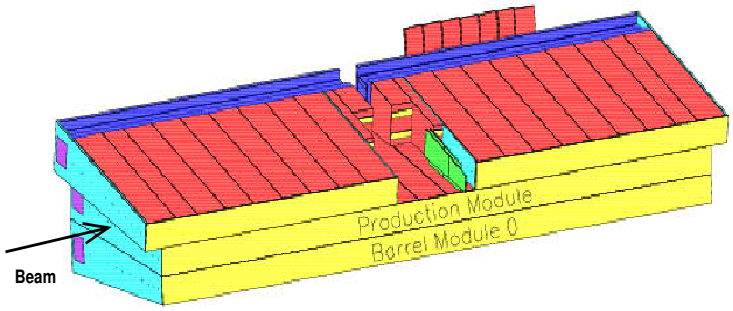

Figure 2: Configuration of the calorimeter modules in the test beam set-up. The arrow indicates the direction of the impinging particles.

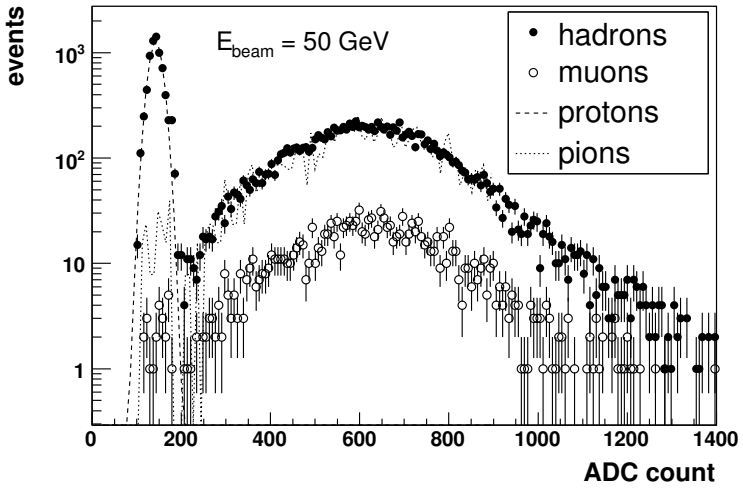

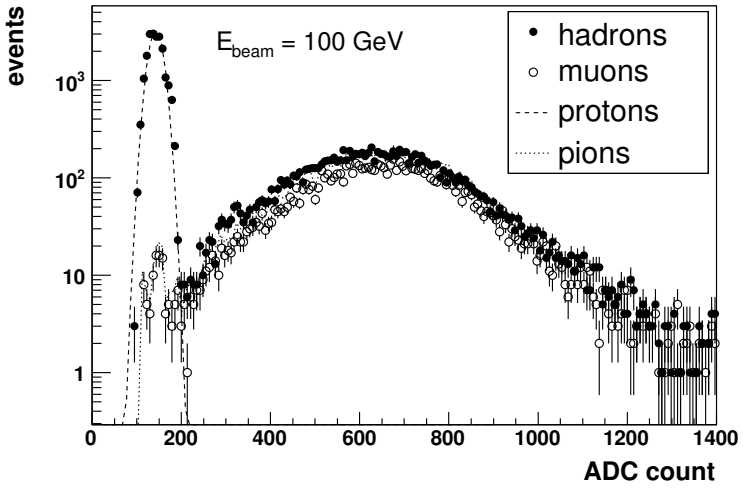

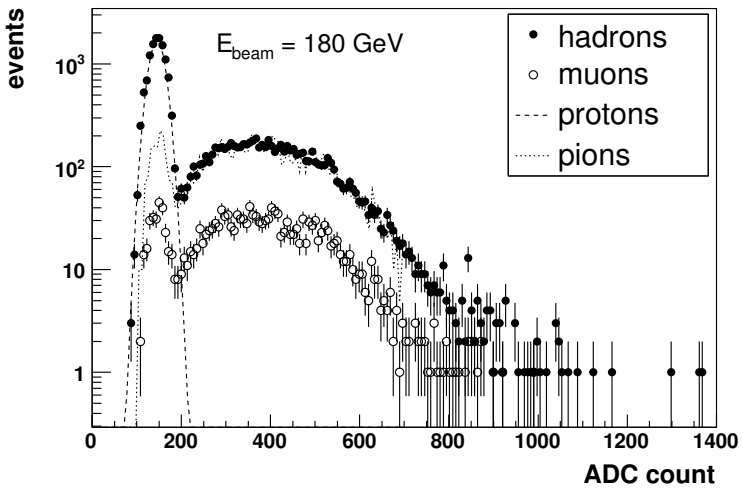

Figure 3: Cherenkov counter response to hadrons and muons at 50, 100 and 180 GeV.

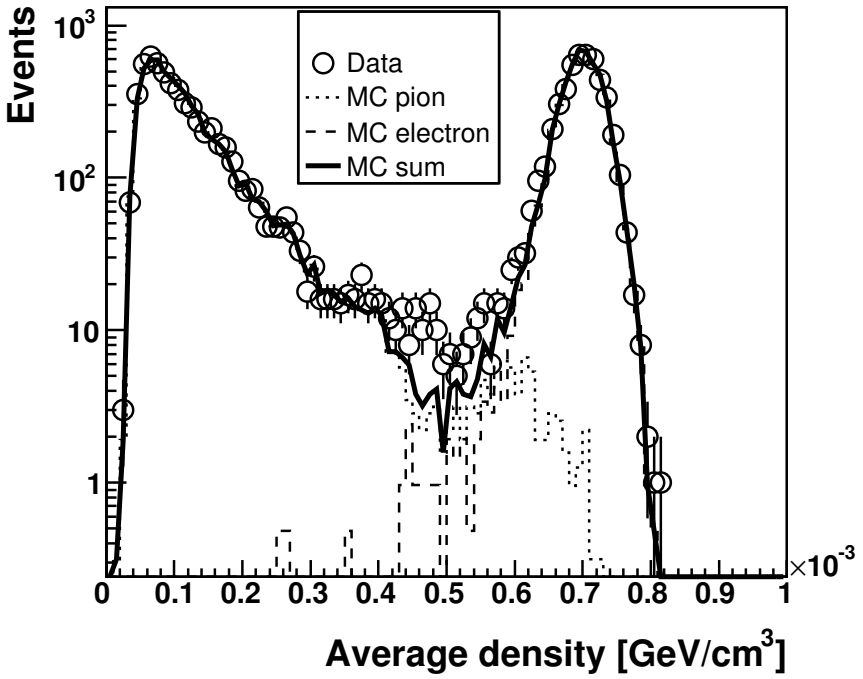

Figure 4: Distribution of the average energy density for $E = 50$ GeV. Shown are data and MC simulations of electrons (dotted line) and pions (dashed line). The solid lines illustrate a fit of the electron and pion MC simulations to the data.

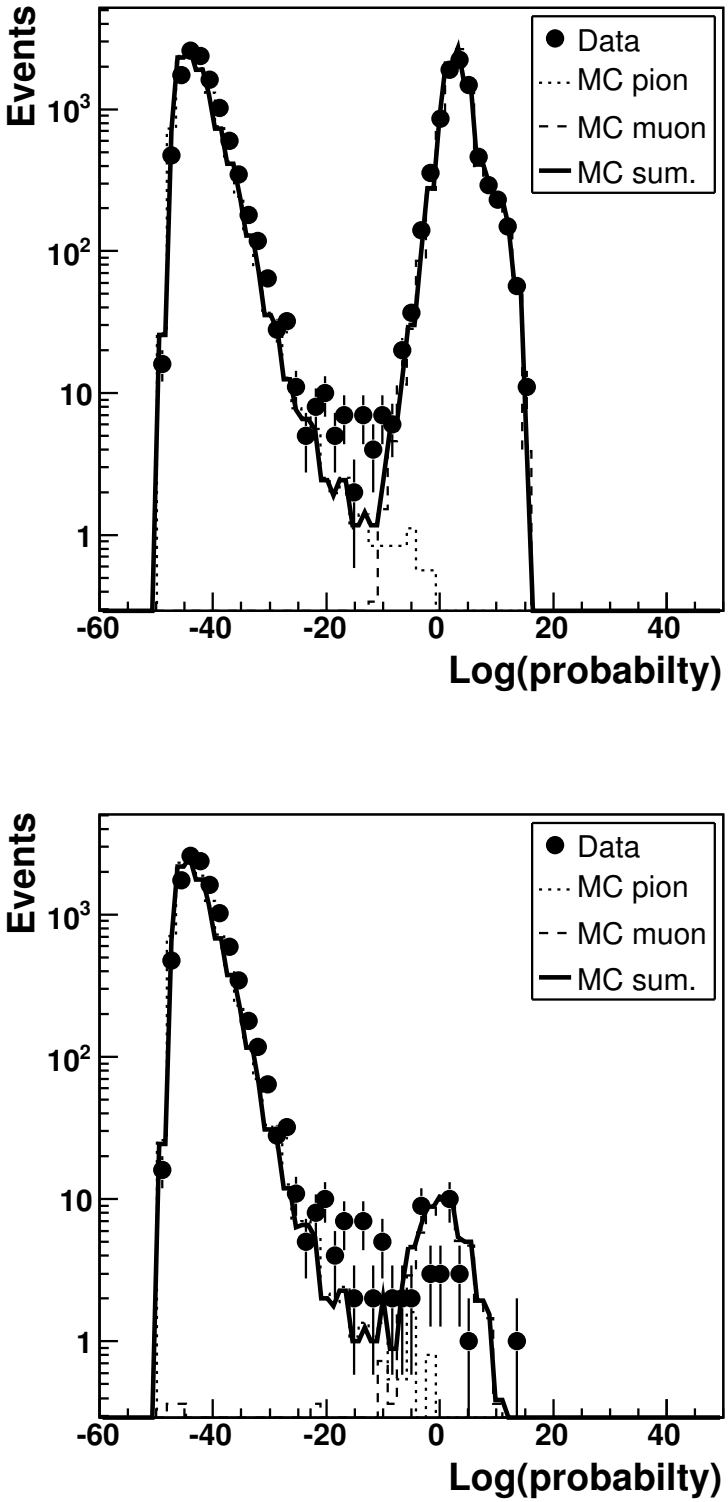

Figure 5: Muon likelihood constructed from the cell energy spectra obtained from simulated muons. In a) all events are shown, in b) only the events passing a cut on the total measured calorimeter energy. Shown are data and MC simulations of pions (dotted line) and muons (dashed line). The solid lines illustrate a fit of the pion and muon MC simulations to the data.

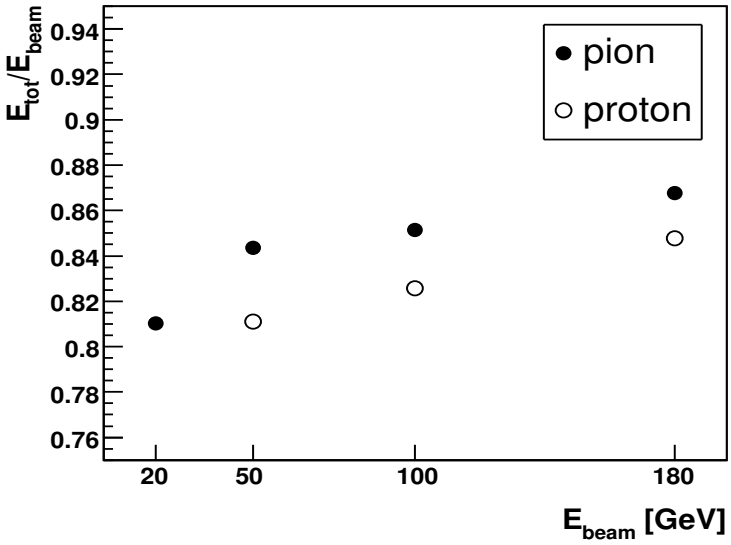

Figure 6: Measured total energy divided by the beam energy for pions (closed circles) and protons (open circles) as a function of the beam energy. The total energy is presented on the electromagnetic energy scale. Only statistical uncertainties are included.

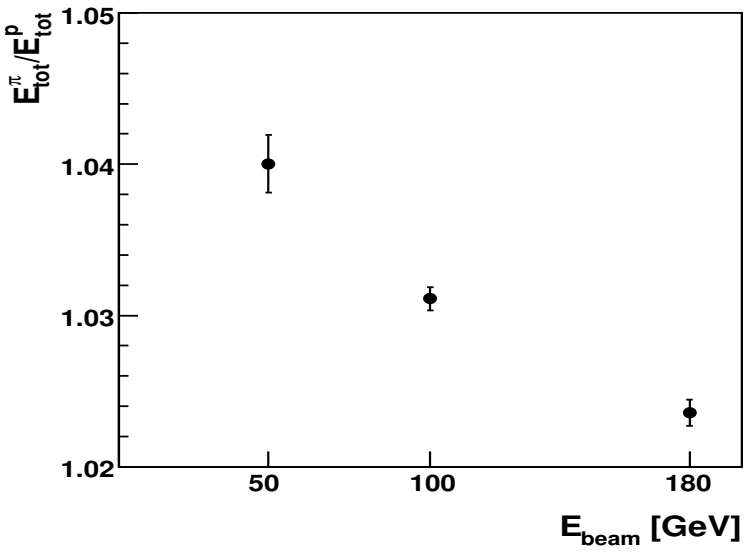

Figure 7: The ratio of the mean energy measured for pions and protons as a function of the beam energy. Only statistical uncertainties are shown.

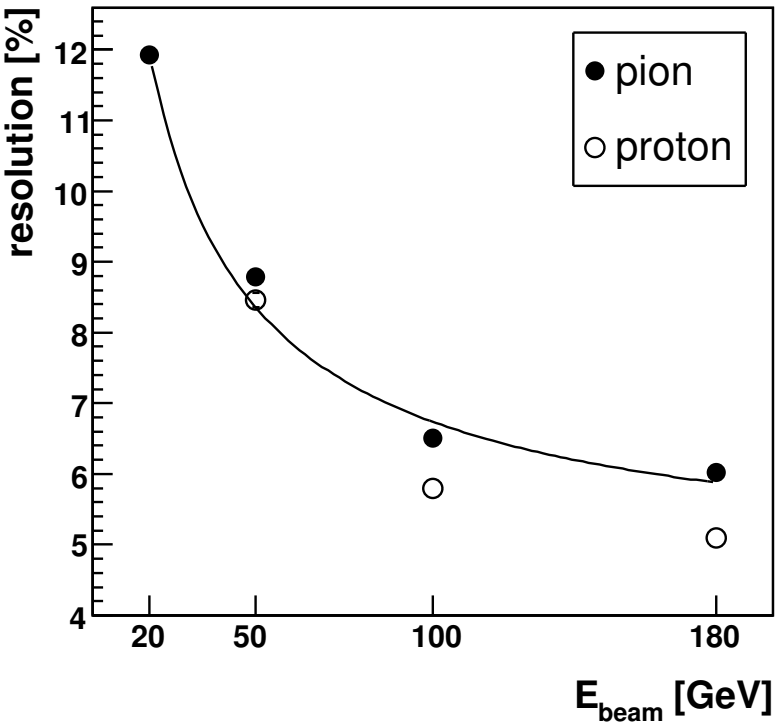

Figure 8: Energy resolution (RMS/E) for pions (open circles) and protons (closed circles) as a function of the beam energy. Overlaid as a curve is a fit to the pion energy resolution. Only statistical uncertainties are included.

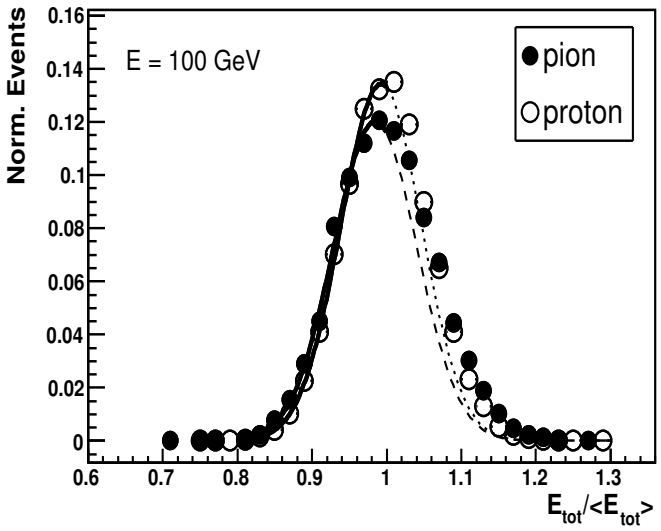

Figure 9: Measured total energy distribution divided by the mean total energy for pions (closed circles) and protons (open circles). Only statistical uncertainties are included.

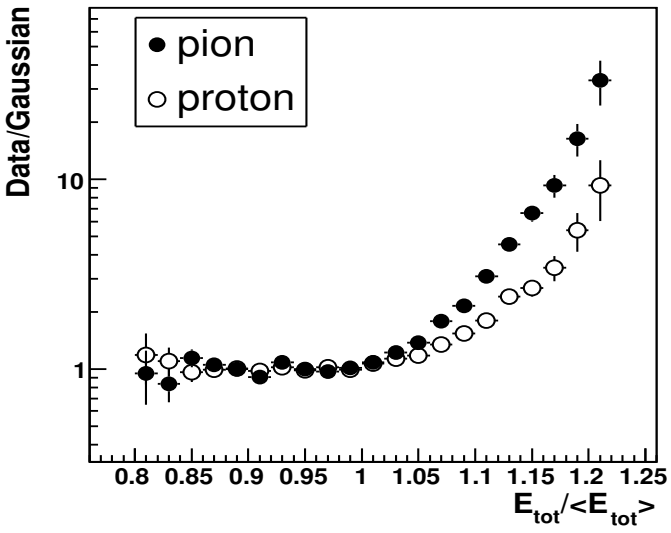

Figure 10: Bin to bin ratio of the reconstructed energy distribution and its Gaussian fit for protons (open circles) and pions (closed circles) as a function of relative reconstructed energy $E_{tot}/\langle E_{tot}\rangle$. The fit was carried out in the region below 1 and extrapolated to the region above 1.

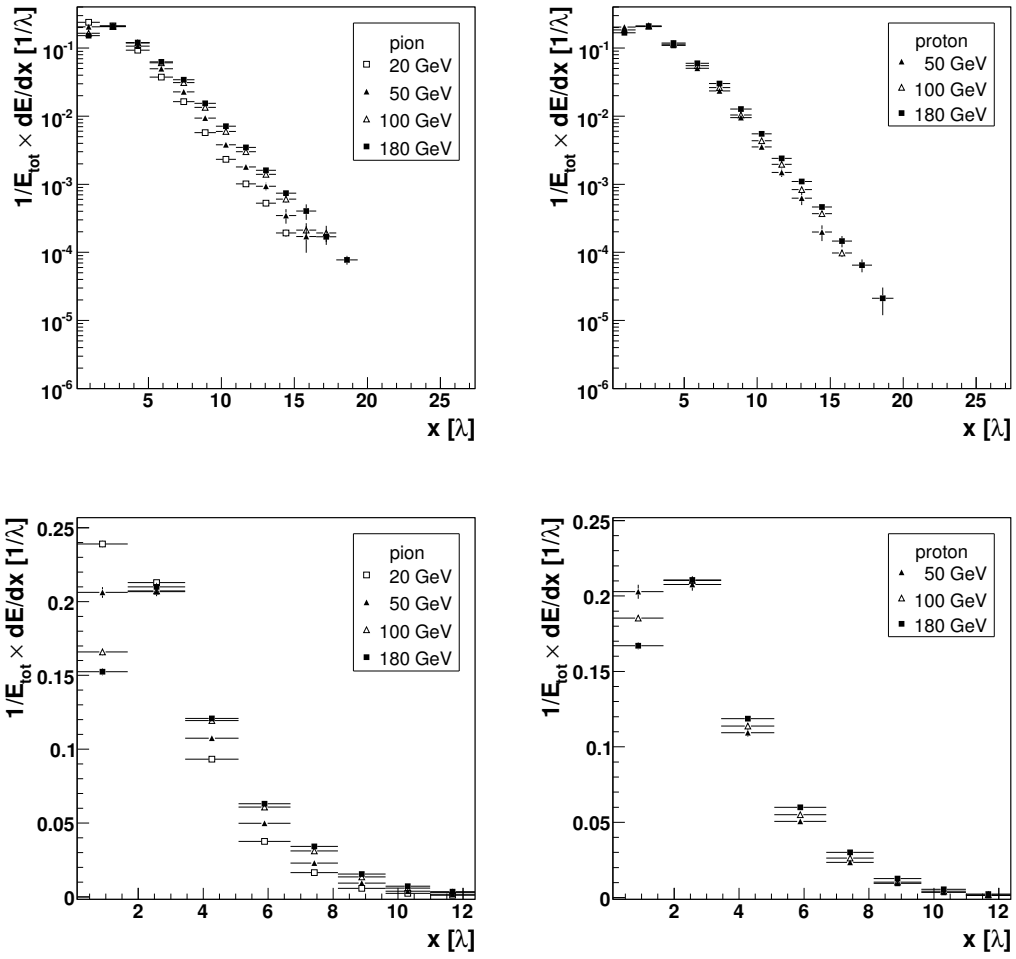

Figure 11: Pion and proton longitudinal shower profile at various energies. In the upper part a logarithmic scale, in the lower part a linear scale is used. Only statistical uncertainties are shown.

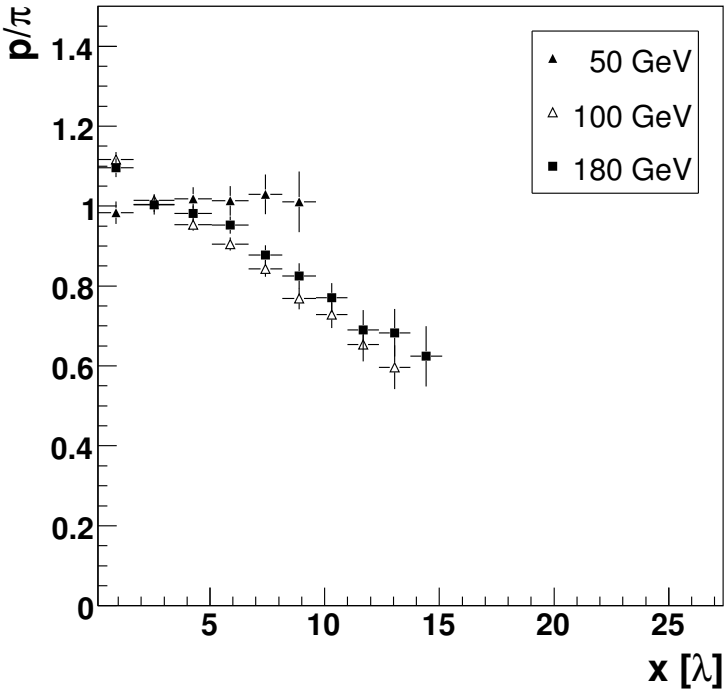

Figure 12: Ratio of the longitudinal profiles for protons and pions at various energies. Only statistical uncertainties are shown.

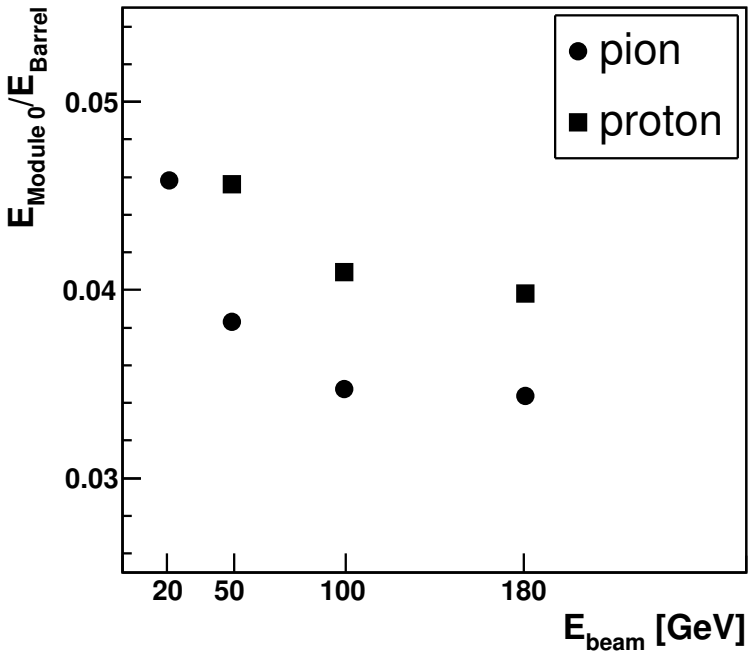

Figure 13: Ratio of energy deposition in the Module 0 and Barrel Module charactering the lateral spread for pion and proton showers as a function of the beam energy. Only statistical uncertainties are included.

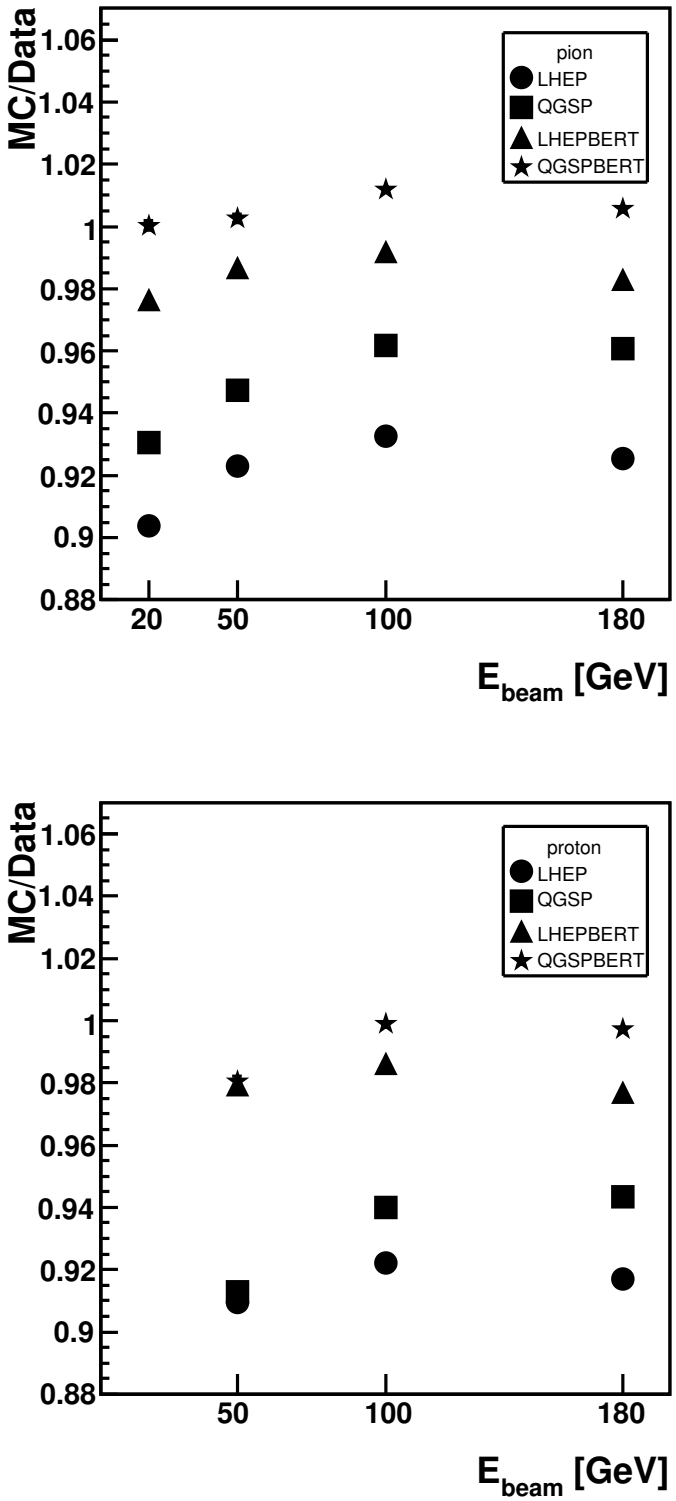

Figure 14: Ratio of the mean energy in the Monte Carlo simulation to the one in the data as a function of the beam energy for four physics list for pions (a) and protons (b). Both data and MC are normalized to the electromagnetic scale. Only statistical uncertainties are included, they are smaller than the marker size.

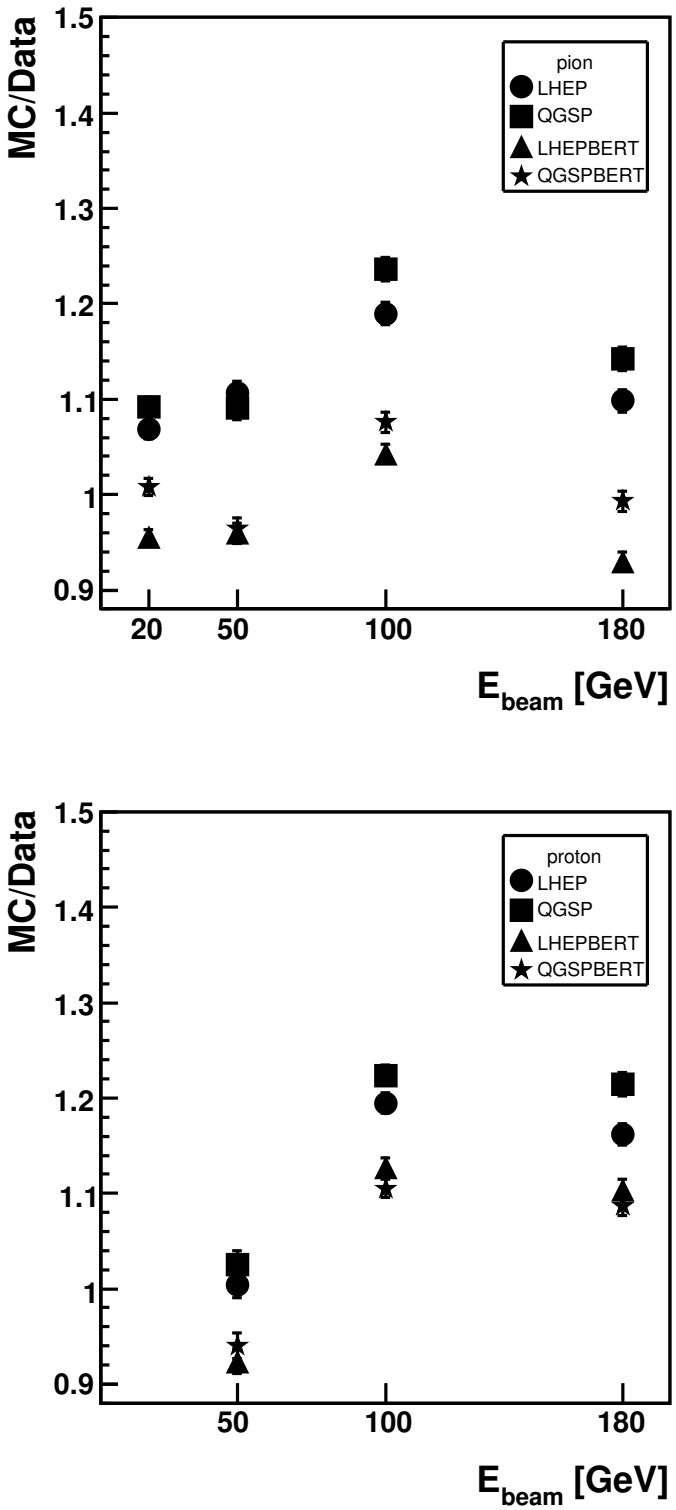

Figure 15: Ratio of the RMS of total energy distribution in the Monte Carlo simulation to one in the data as a function of the beam energy for four physics list for pions (a) and protons (b). Only statistical uncertainties are included.

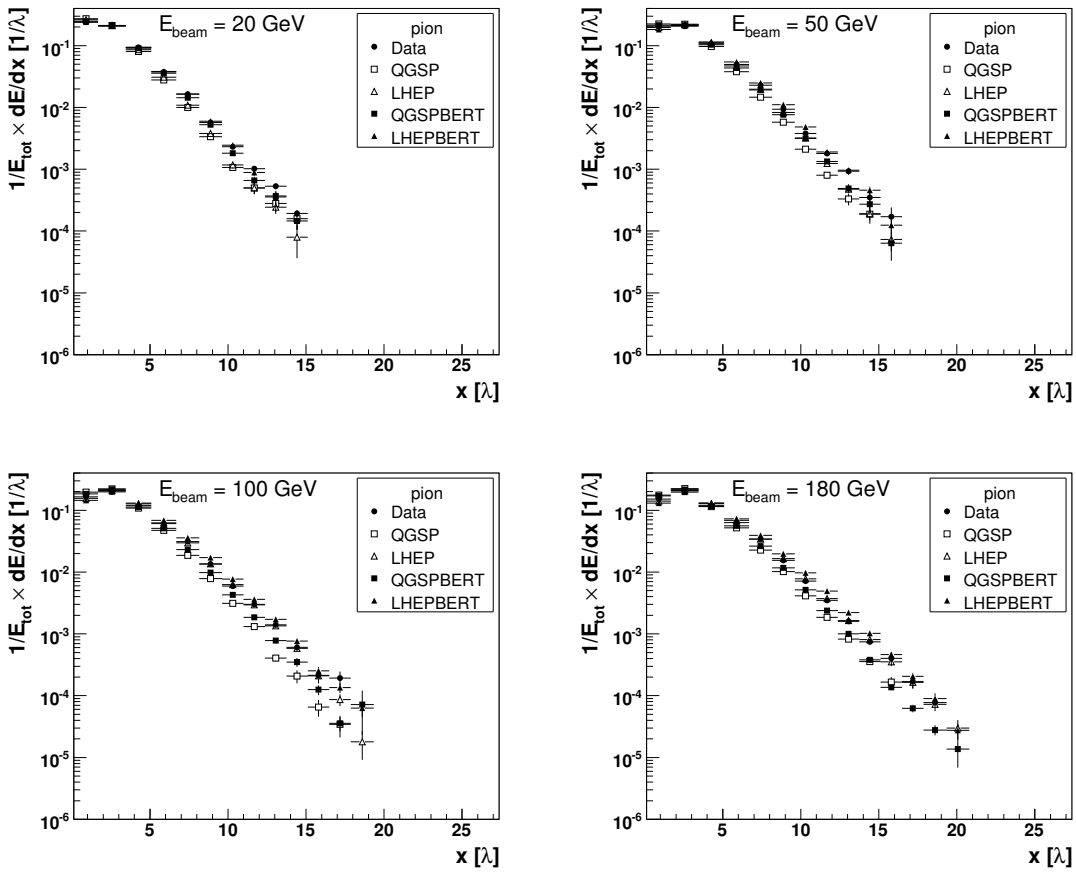

Figure 16: Pion longitudinal shower profiles at various beam energy compared in data and various MC simulations. Only statistical uncertainties are shown.

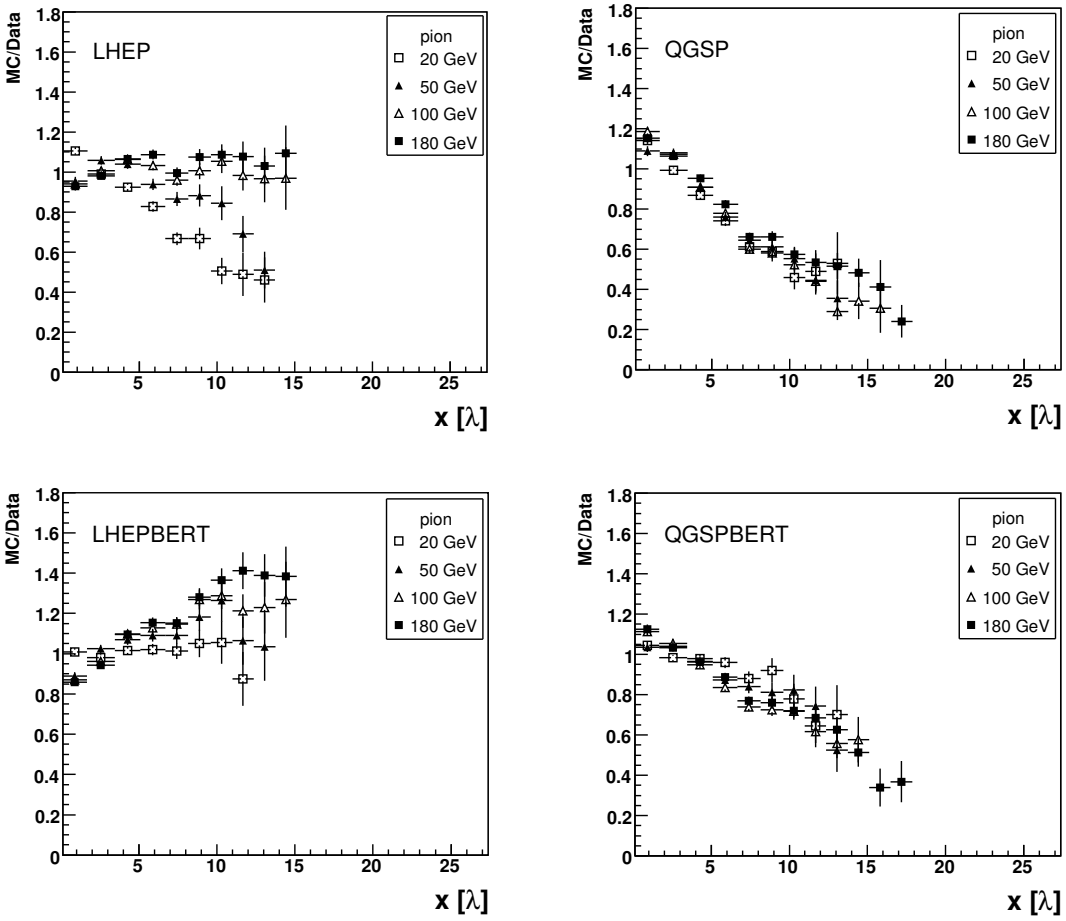

Figure 17: Ratio of various MC simulations to data for the Pion longitudinal shower profile description at various energies. Only statistical uncertainties are shown.

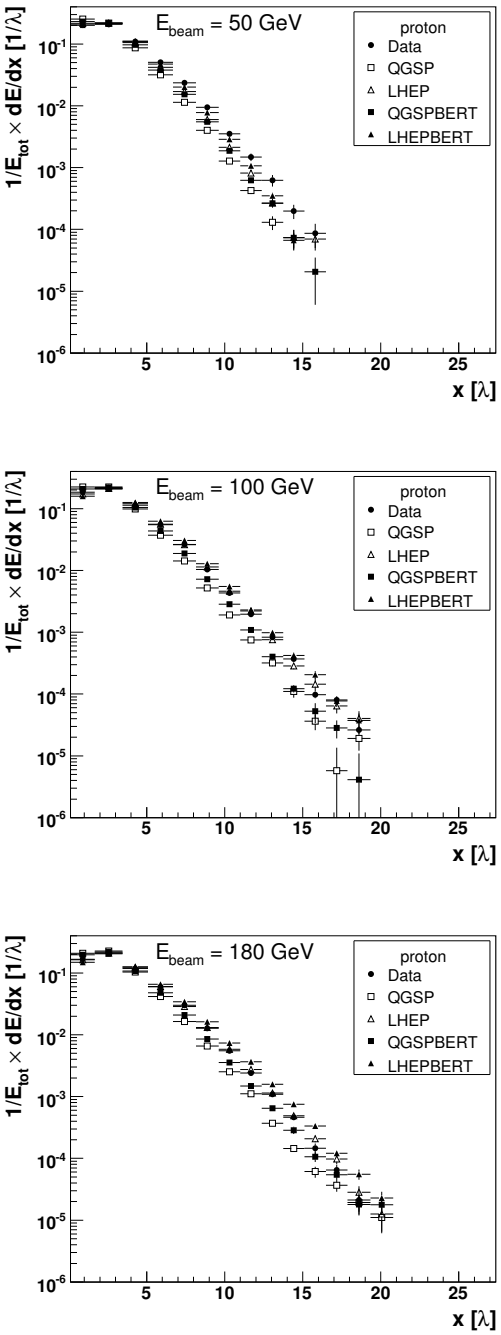

Figure 18: Proton longitudinal shower profile at various beam energy compared for data and for various MC simulations. Only statistical uncertainties are shown.

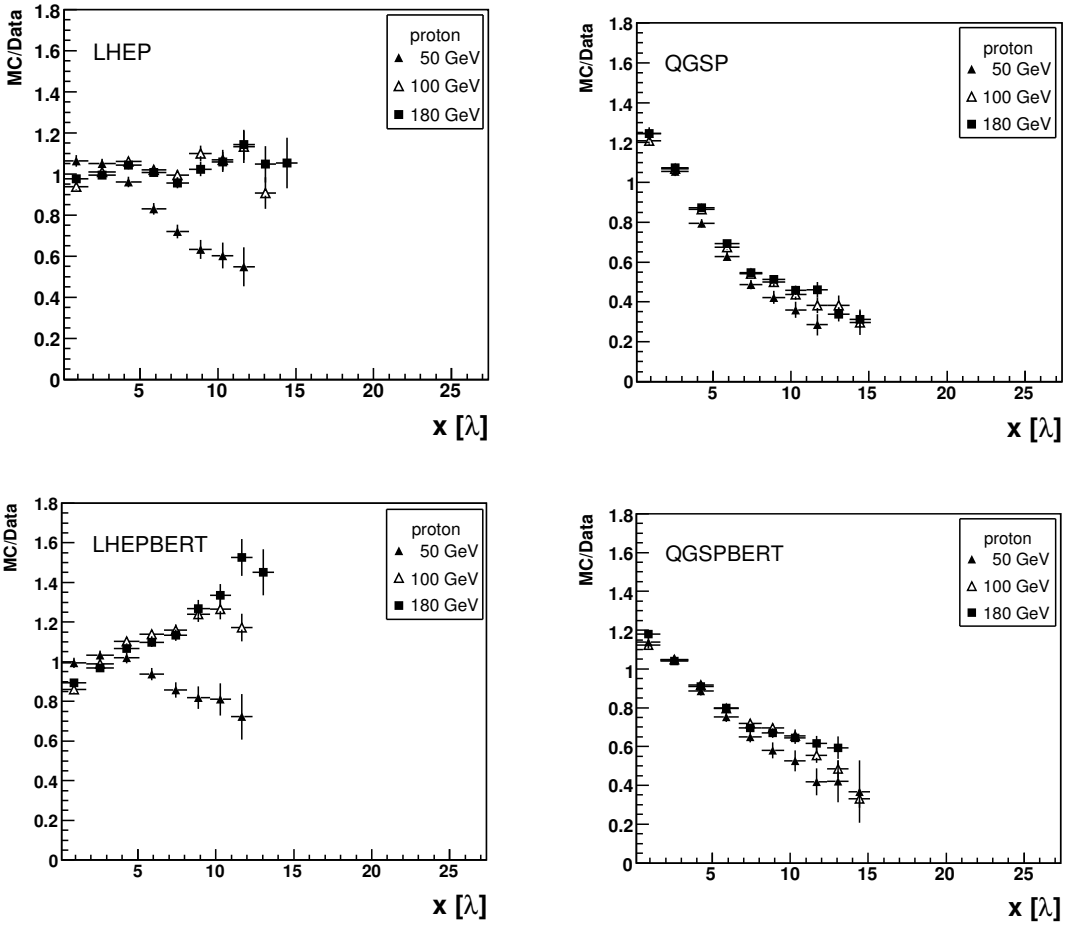

Figure 19: Ratio of various MC simulations to data for the Pion longitudinal shower profile description at various energies. Only statistical uncertainties are shown.

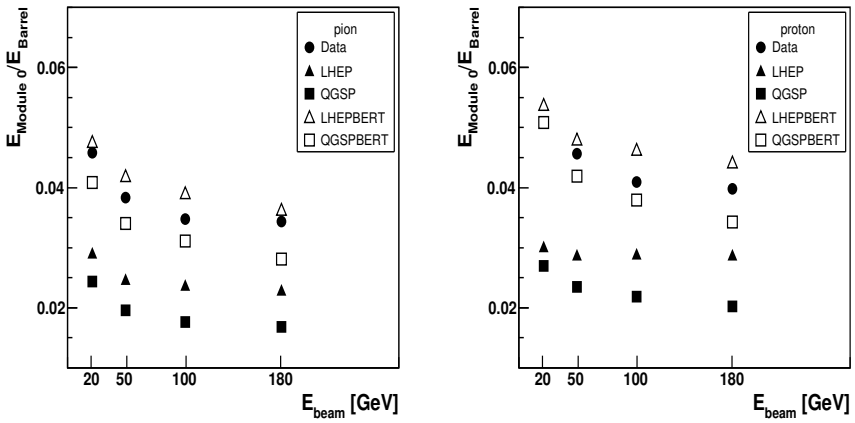

Figure 20: Ratio of energy deposition in the Module 0 and the Barrel Module for data and for various MC simulations as a function of the beam energy. Only statistical uncertainties are shown.

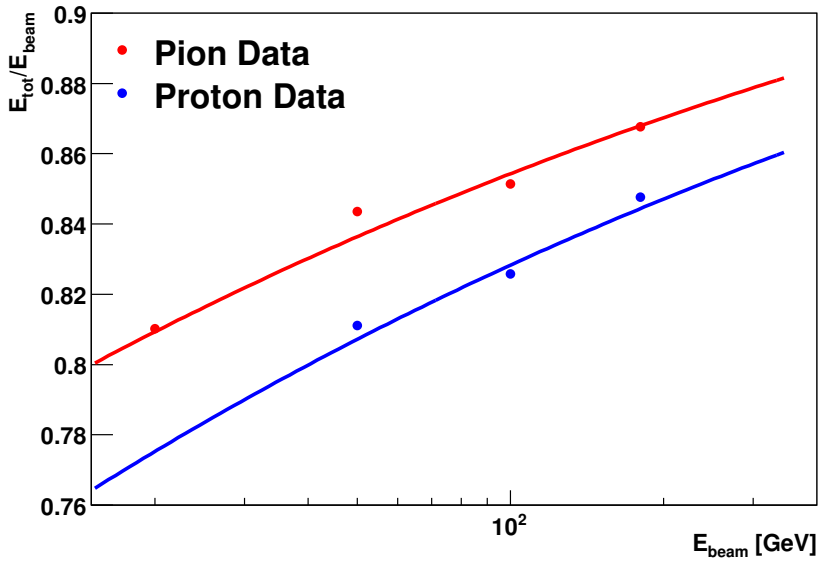

Figure 21: Pion and proton response as a function of the beam energy. Overlaid is a fit to a parameterisation describing the energy response of pions and protons given in eq. 3. The total energy is presented on the electromagnetic energy scale. Only statistical uncertainties are included in the data points.

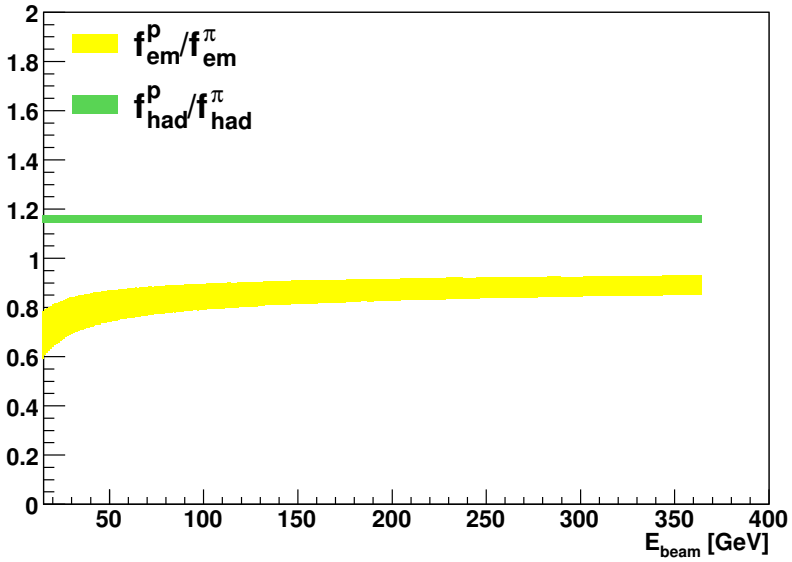

Figure 22: Ratio of electromagnetic (light band) and hadronic (dark band) energy fraction of proton and pions as a function of the beam energy. The bands indicate the uncertainty due to the uncertainty of the fit parameters.

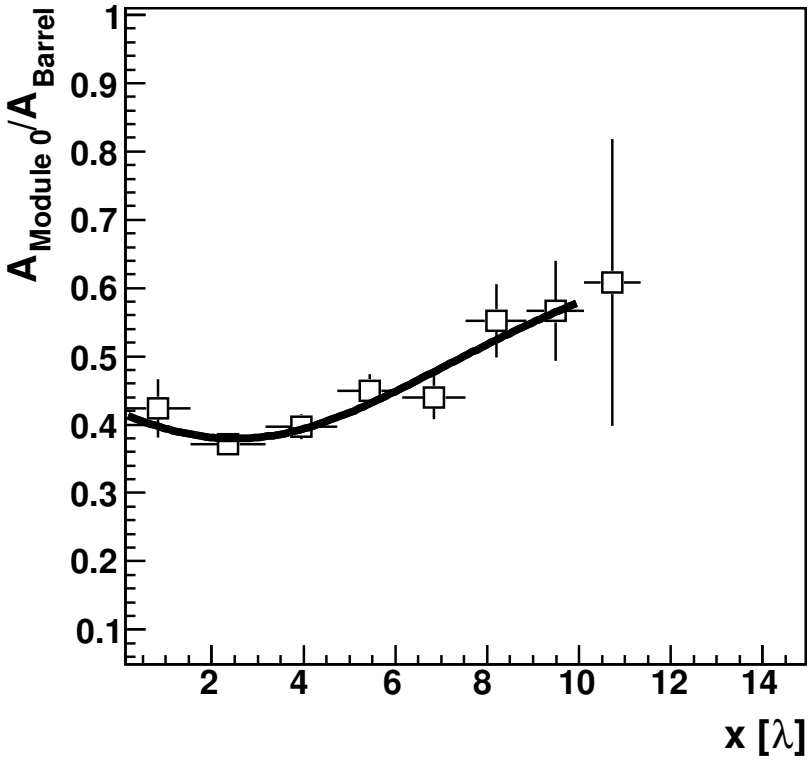

Figure 23: Ratio of the energy depositions in the A samplings of the Module 0 and the Barrel module.

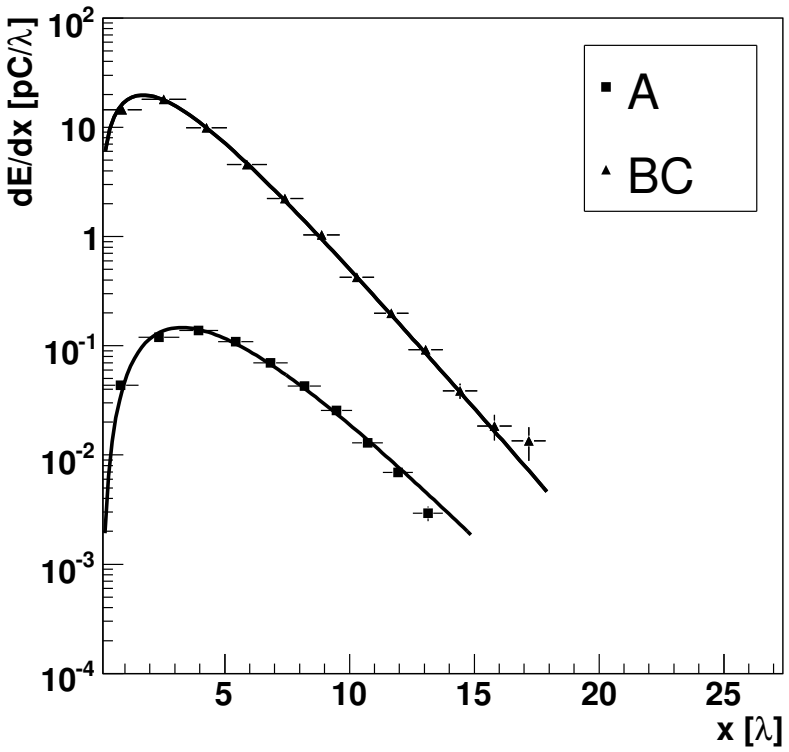

Figure 24: Longitudinal shower profile of 100 GeV pions measured in the BC and A sampling of the Barrel module. Only statistical uncertainties are shown. In most case statistical uncertainties are smaller than the marker size. Overlaid as line is a parameterisation of the mean longitudinal shower profile for the part of the shower developing in the A cell.

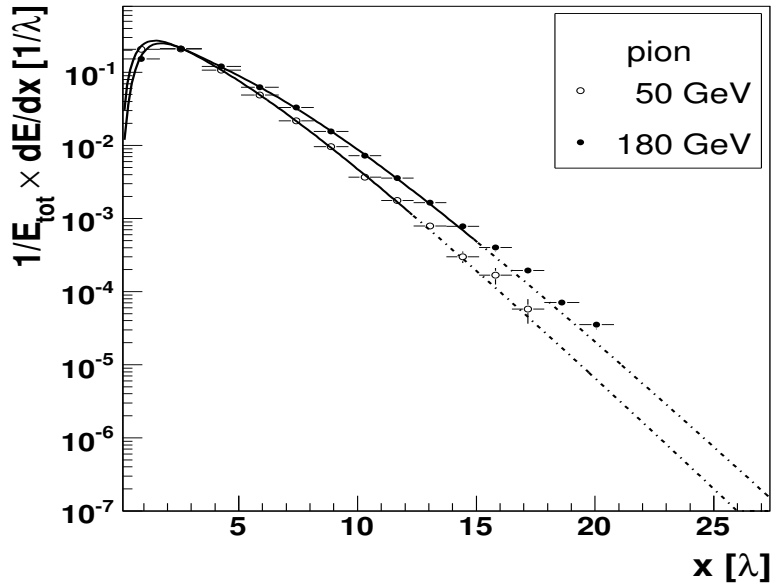

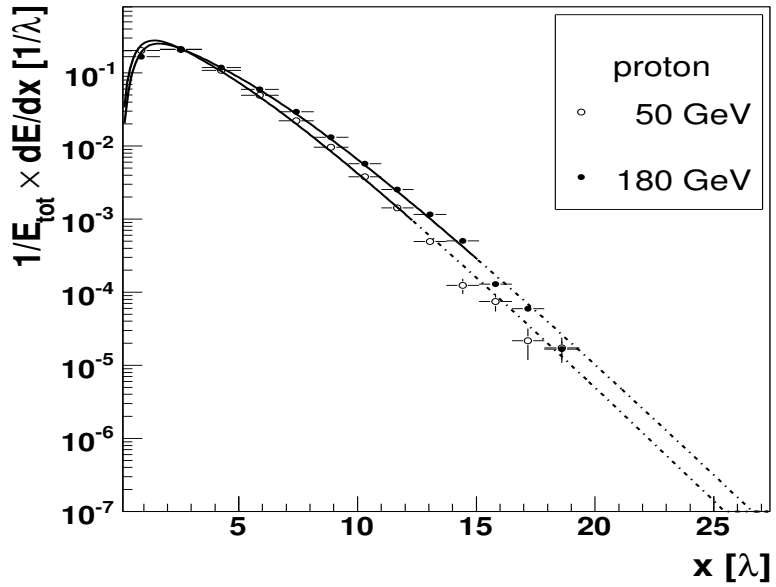

Figure 25: Unfolded longitudinal shower profile for pions and protons at 50 and 180 GeV. Superimposed is the result of the analytical shower parameterisation adjusted to the data. The solid line indicates the region where the fit is done, the dashed line indicates the extrapolation outside this region.

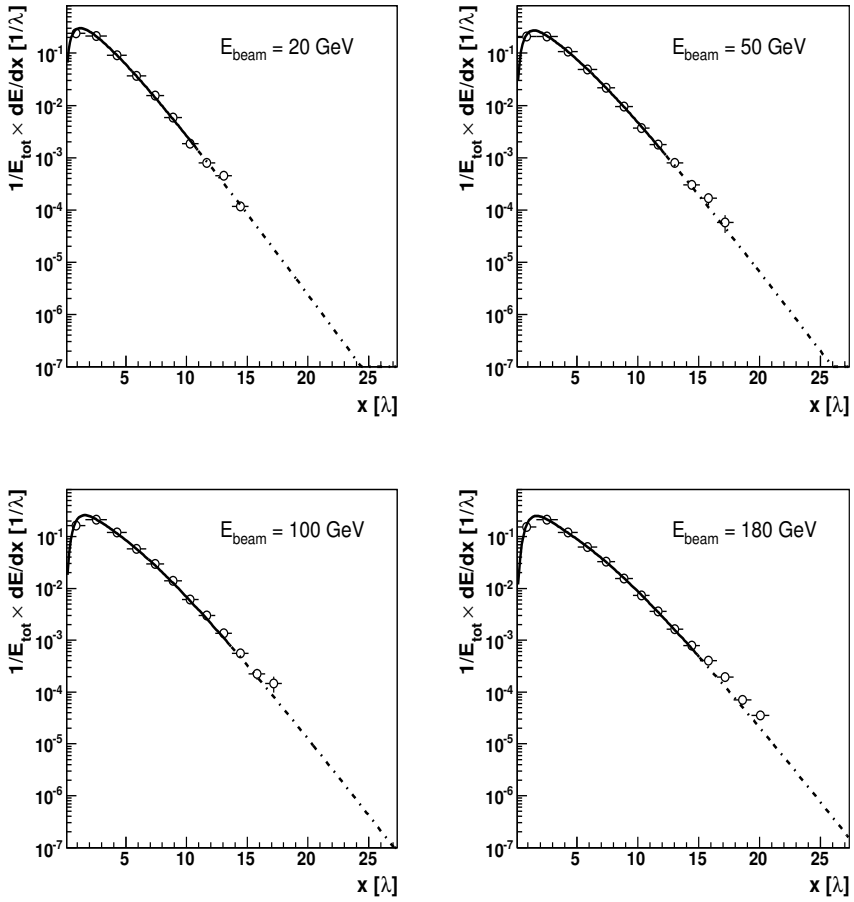

Figure 26: Unfolded longitudinal shower profile for pions at 20, 50, 100 and 180 GeV. Superimposed is the result of the analytical shower parameterisation adjusted to the data. The solid line indicates the region where the fit is done, the dashed line indicates the extrapolation outside this region.

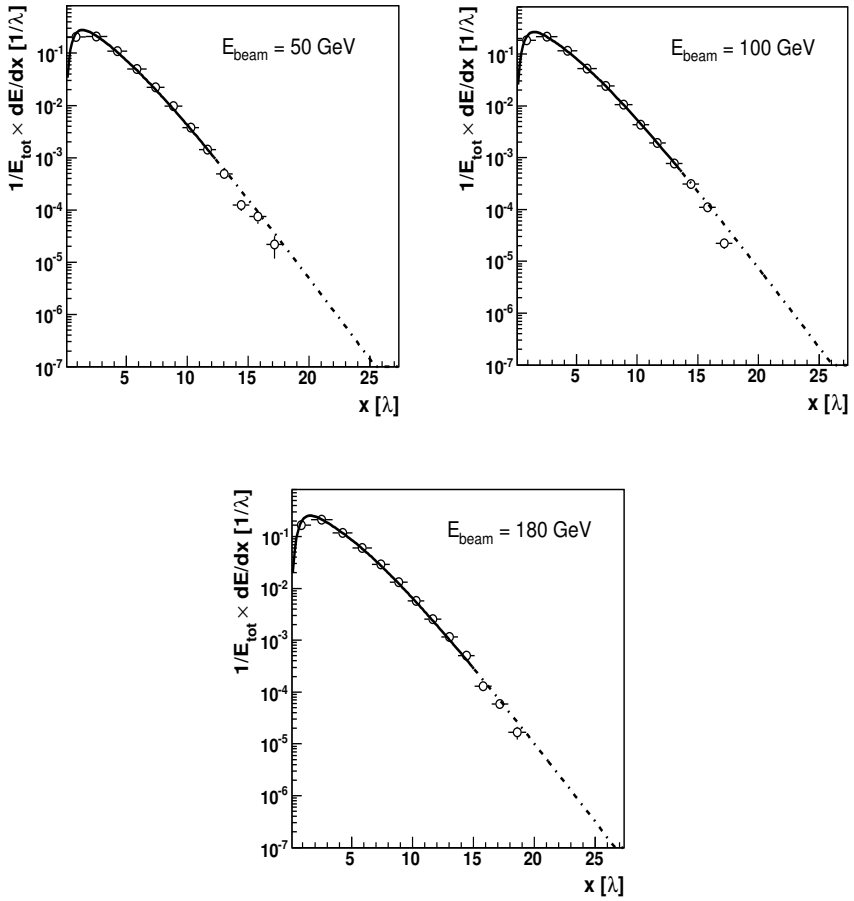

Figure 27: Unfolded longitudinal shower profile for protons at 50, 100 and 180 GeV. Superimposed is the result of the analytical shower parameterisation adjusted to the data. The solid line indicates the region where the fit is done, the dashed line indicates the extrapolation outside this region.

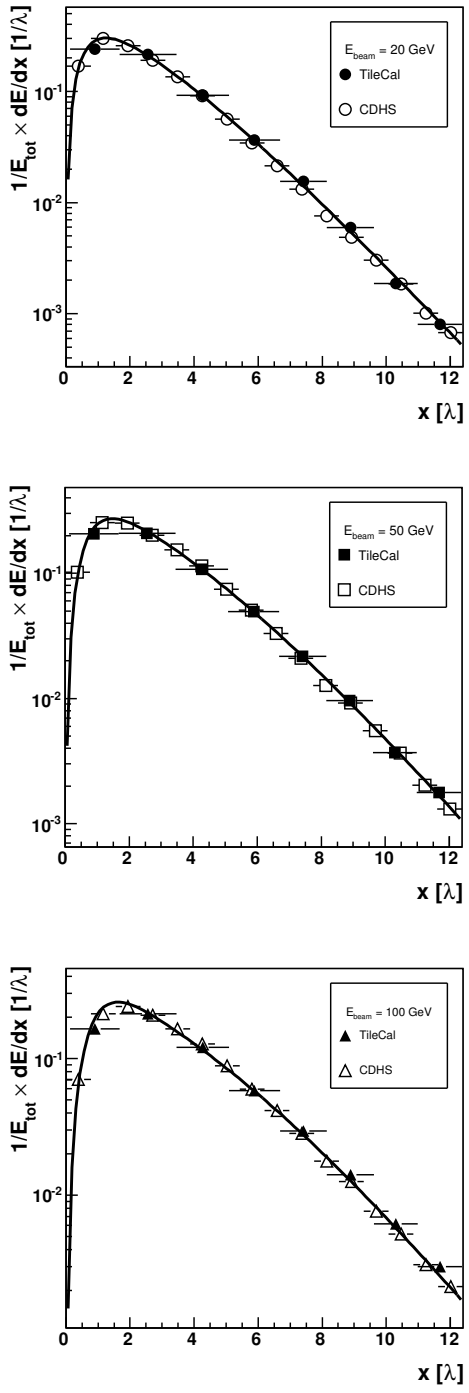

Figure 28: Comparison of pion longitudinal shower profile measured with TileCal and CDHS calorimeter at various energies. The results of fit to TileCal data are also presented.

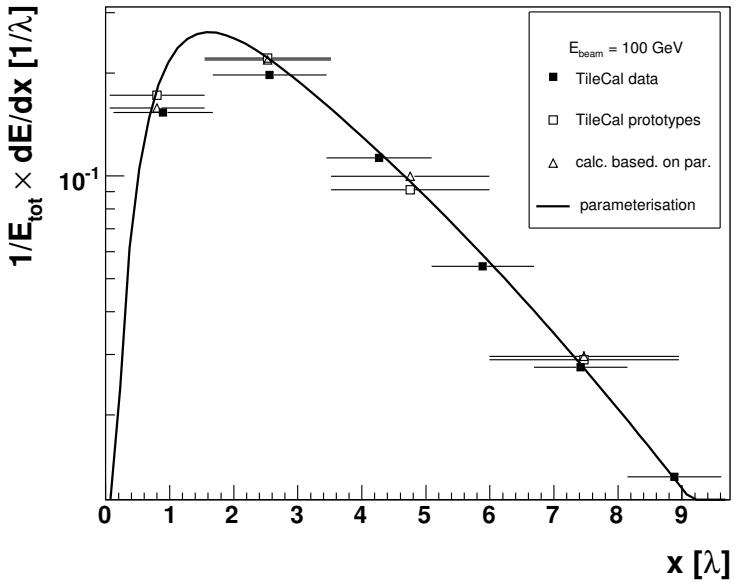

Figure 29: Comparison of 100 GeV pion longitudinal shower profile measured with TileCal prototype and production modules. Triangles are the result of integration of the parameterisation within each bin of measurement with prototype modules divided by the bin width.

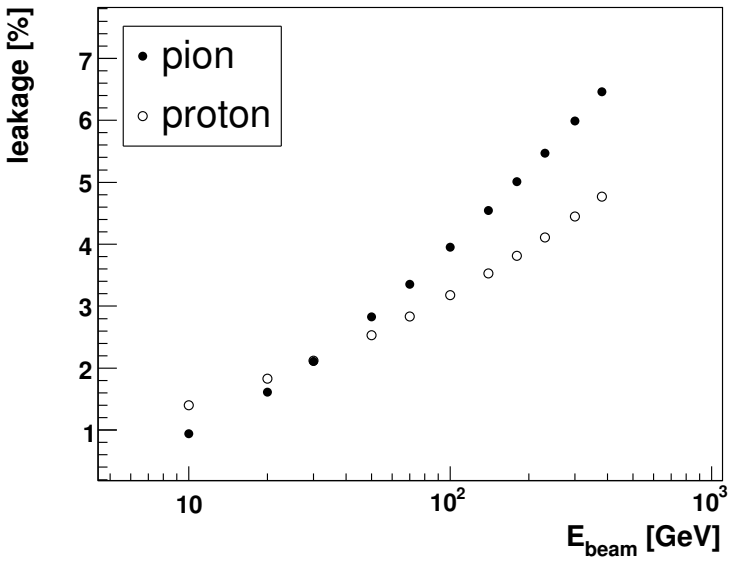

Figure 30: Calculated average longitudinal energy leakage fraction from TileCal production modules for pions (closed symbols) and protons (open symbols) corresponding to the nominal TileCal length in the projective geometry for a particle incident at $|\eta| = 0.35$.

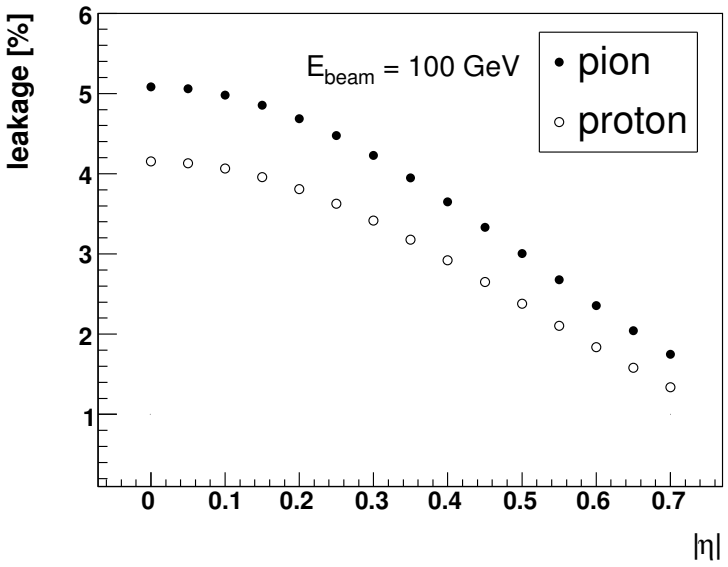

Figure 31: Calculated average longitudinal energy leakage fraction for pions (closed symbols) and protons (closed symbols) at 100 GeV as a function of the calorimeter depth expressed in units of $|\eta|$ corresponding to the nominal TileCal length in the projective geometry.

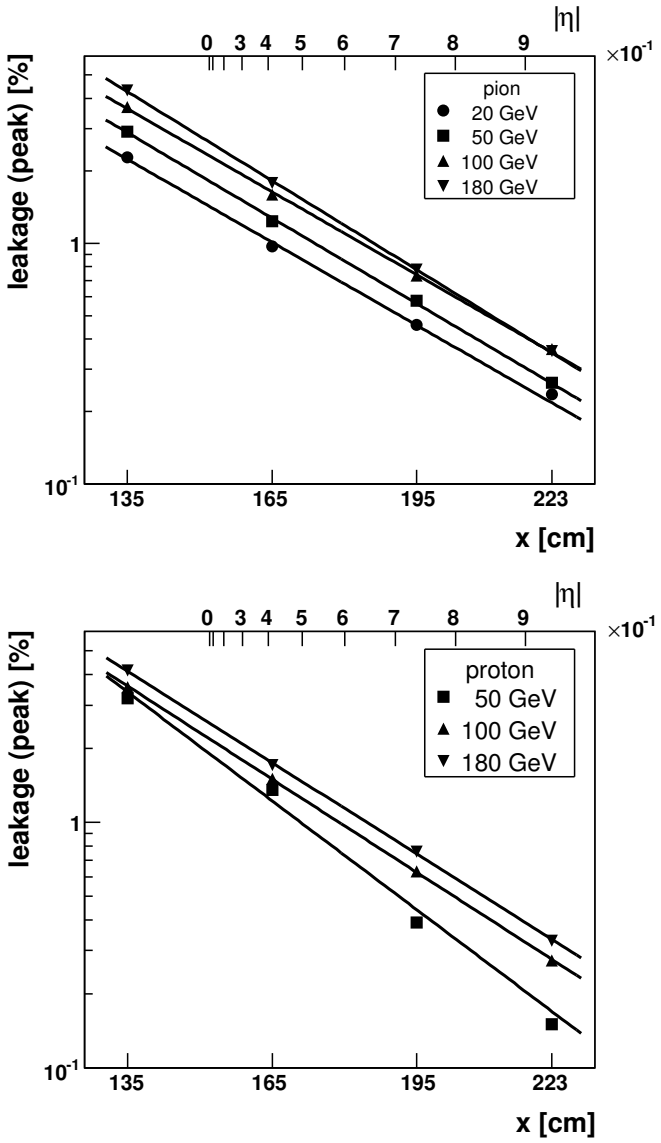

Figure 32: Calculated longitudinal peak energy leakage fraction on the deposited energy measured by the mean of a Gaussian fit ("peak") for 20, 50, 100 and 180 GeV pions (a) and protons (b) as a function of the calorimeter length. The symbols refer to the measurements, the lines indicate a parameterisation. The $|\eta|$ values to which the calorimeter length corresponds to in projective geometry is indicated on top of the figure.

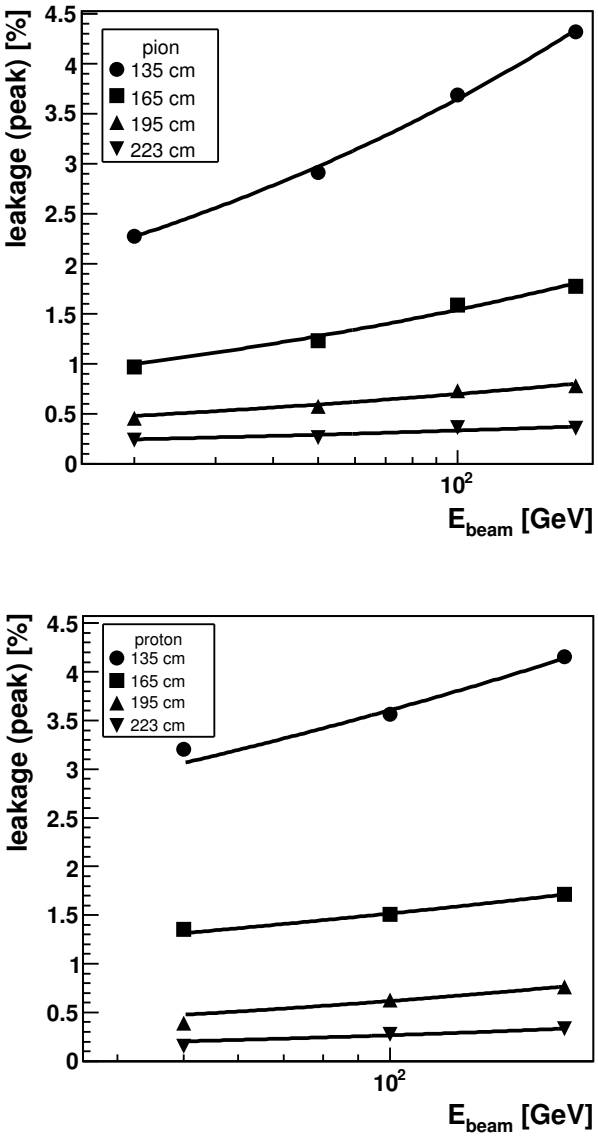

Figure 33: Calculated longitudinal energy leakage on the deposited energy measured by the mean of a Gaussian fit ("peak") for various depths for pions (a) and for protons (b) as a function of beam energy. Superimposed as lines is a parameterisation described in the text.

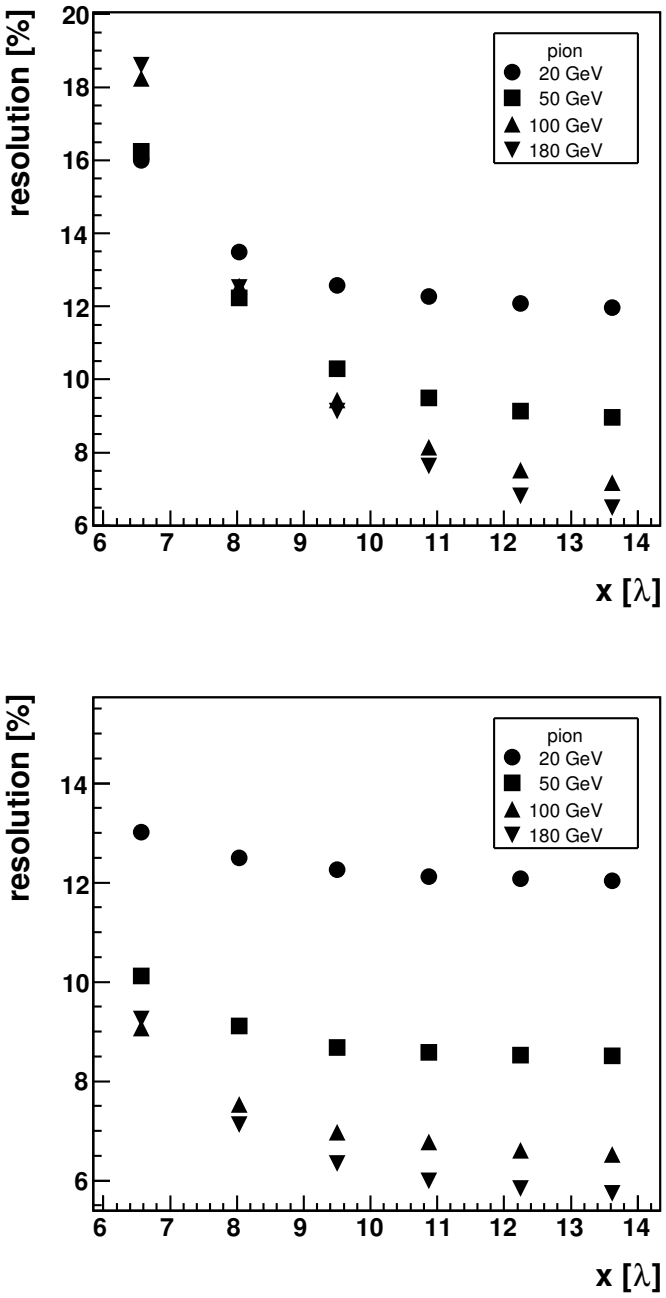

Figure 34: The dependence of the energy resolution of TileCal to pions on the depth of the calorimeter. The resolution is defined as RMS/mean of the total energy distribution in the upper plot and in the bottom one it is defined as σ/peak of a Gaussian fit to the distribution in the range -2σ to 2σ around the peak value.

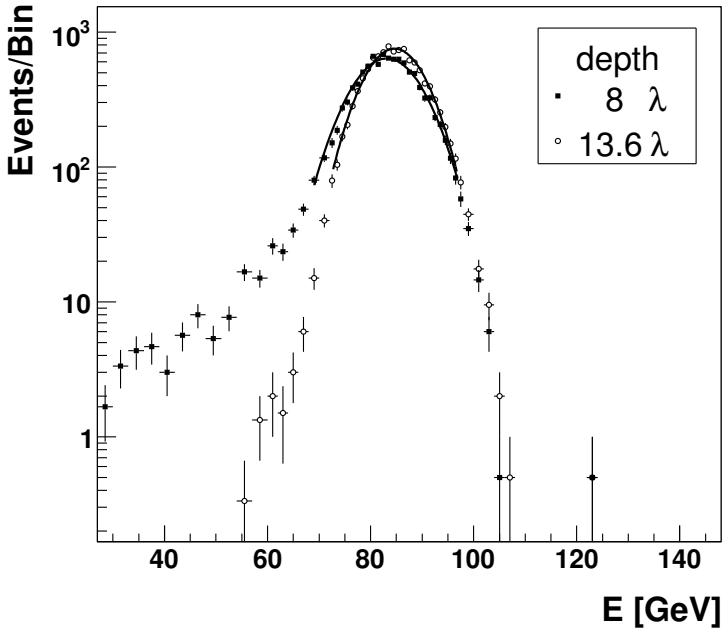

Figure 35: The total energy distributions of 100 GeV pions for two depths of the calorimeter. The superimposed lines are the results of a fit to the energy distributions in the range -2σ to 2σ around the peak value.